High-dimensional imaging of the HPV-induced tumor microenvironment to improve clinical outcomes

Abdulrahman, Z.

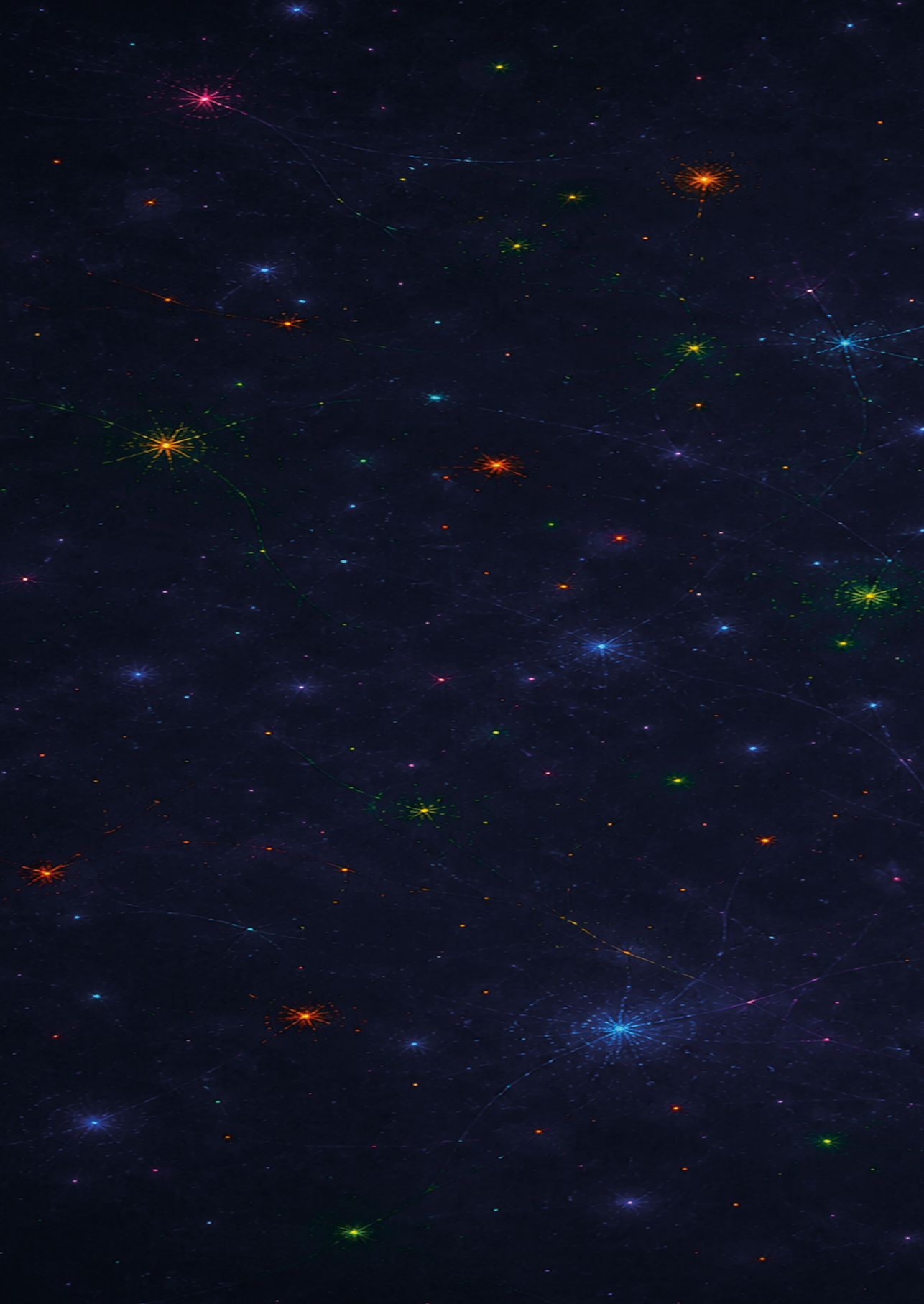

Chapter 8

Tumor-specific T cells support chemokine-driven spatial organization of intratumoral immune microaggregates needed for long survival

Ziena Abdulrahman, Saskia J. Santegoets, Gregor Sturm, Pornpimol Charoentong, Marieke E. IJsselsteijn, Antonios Somarakis, Thomas Höllt, Francesca Finotello, Zlatko Trajanoski, Sylvia L. van Egmond, Dana A.M. Mustafa, Marij J.P. Welters, Noel F.C.C. de Miranda, Sjoerd H. van der Burg

Journal for ImmunoTherapy of Cancer 2022

Graphical abstract

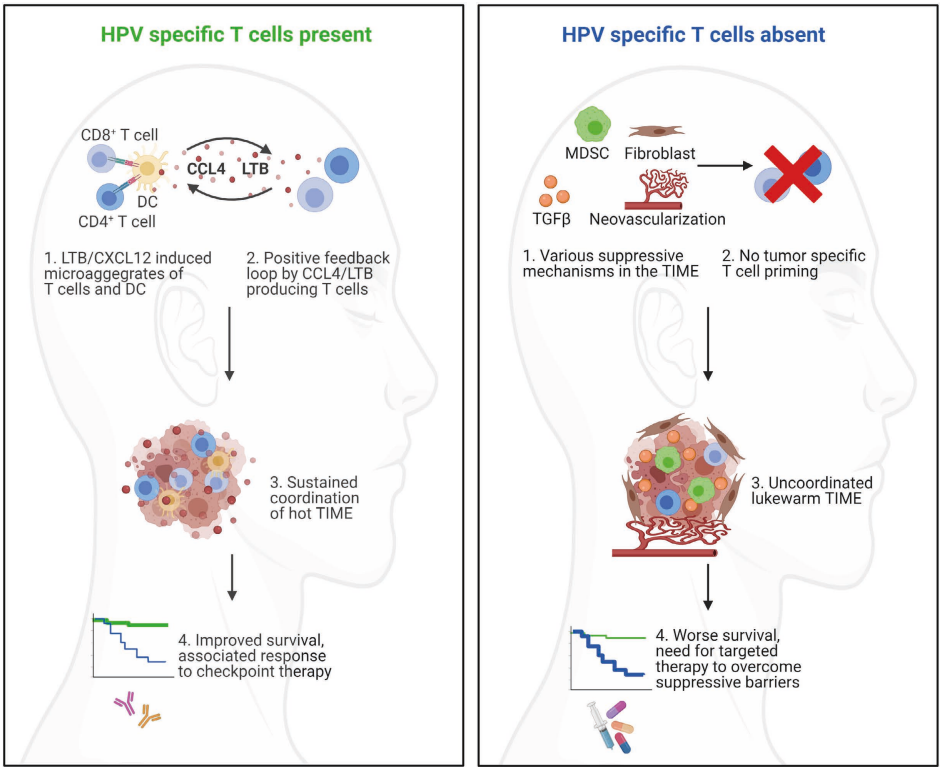

Key findings

- A specific spatial phenotypic signature (SPS) portrays long surviving oropharyngeal cancer patients.
- The SPS consists of intratumoral T cell and dendritic cell microaggregates.
- Chemokines produced by tumor-specific T cells sustain the orchestration of the SPS.
- Patients lacking this SPS express multiple targetable immunosuppressive mechanisms.

Abstract

Background

The composition of the tumor immune microenvironment (TIME) associated with good prognosis generally also predicts the success of immunotherapy, and both entail the presence of pre-existing tumor-specific T cells. Here, the blueprint of the TIME associated with such an ongoing tumor-specific T cell response was dissected in a unique prospective oropharyngeal squamous cell carcinoma (OPSCC) cohort, in which tumor-specific tumor-infiltrating T cells were detected (IR^+) or not (IR^-).

Methods

A comprehensive multi-modal, high-dimensional strategy was applied to dissect the TIME of treatment naive IR^+ and IR^- OPSCC tissue, including bulk RNA sequencing by NanoString, imaging mass cytometry (Hyperion) for phenotyping and spatial interaction analyses of immune cells, and combined single-cell gene expression profiling and T cell receptor sequencing (scRNAseq) to characterize the transcriptional states of clonally expanded tumor-infiltrating T cells.

Results

IR^+ patients had an excellent survival during >10 years follow-up. The tumors of IR^+ patients expressed higher levels of genes strongly related to IFNγ signaling, T-cell activation, T-cell receptor signaling, and mononuclear cell differentiation as well as genes involved in several immune signaling pathways, than IR^- patients. The top differently overexpressed genes included CXCL12 and LTB, involved in ectopic lymphoid structure development. Moreover, scRNAseq not only revealed that $CD4^+$ T cells were the main producers of LTB, but also identified a subset of clonally expanded $CD8^+$ T cells, dominantly present in IR^+ tumors, which secreted the T cell and dendritic cell (DC) attracting chemokine CCL4. Indeed, immune cell infiltration in IR^+ tumors is stronger, highly coordinated and has a distinct spatial phenotypic signature, characterized by intratumoral microaggregates of $CD8^+CD103^+$ and $CD4^+$ T cells with DCs. In contrast, the IR^- TIME comprised spatial interactions between lymphocytes and various immunosuppressive myeloid cell populations. The impact of these chemokines on local immunity and clinical outcome was confirmed in an independent The Cancer Genome Atlas OPSCC cohort.

Conclusion

The production of lymphoid cell attracting and organizing chemokines by tumor-specific T cells in IR$^+$ tumors constitutes a positive feedback loop to sustain the formation of the DC-T-cell microaggregates and identifies patients with excellent survival after standard therapy.

Introduction

Head and neck cancer is the sixth most prevalent cancer type and predominantly comprises squamous cell carcinoma (90%).[1] Head and neck tumors can develop in the pharynx, larynx, oral cavity and sinonasal tract following genetic alterations driven by carcinogen exposure or high-risk human papillomavirus (HPV) infection. The majority of oropharyngeal squamous cell carcinomas (OPSCC), which include tumors of the tonsils and the base of tongue, are induced by HPV type 16 (HPV16).[2] Patients with HPV16$^+$ OPSCC display a longer overall survival (OS) and a lower recurrence rate after surgery and/or chemoradiation than patients with HPV$^-$ OPSCC.[3] Head and neck squamous cell carcinomas (HNSCC) are generally treated with surgery and/or chemo-radiation [4], associated with high comorbidities and thereby severely impacting patients' quality of life. Immune checkpoint inhibition (ICI) is nowadays used in recurrent or metastatic HNSCC after failure of first line treatment, and is only successful in 20-30% of patients.[5 6] The low response rate to ICI highlights the need to better understand the complex biology underlying the state of the tumor immune microenvironment (TIME) in HNSCC, in order to improve the efficacy of ICI and to provide a rationale for new immunotherapy design.

Biomarker studies of the TIME suggest that parameters associated with good prognosis also predict the efficacy of ICI, and both entail the strong presence of pre-existing CD4$^+$ and CD8$^+$ tumor-reactive T cells.[7-10] In most types of tumors it is difficult to assess the presence of tumor-reactive tumor infiltrating lymphocytes (TILs) as it requires the identification of tumor (neo)antigens recognized by T cells for each individual patient. Consequently, it will be tough to identify the immunological blueprint of a productive – i.e. a tumor-reactive T cell-infiltrated – TIME, and subsequently to pinpoint what issues should be addressed by novel immunotherapy approaches. In the case of HPV16-induced OPSCC all tumors have the HPV neoantigens in common, providing a unique setting to unravel the make-up of a productive TIME.

Here, we made use of a unique prospective cohort of OPSCC patients to address these questions. We recently showed that the improved survival of HPV16$^+$ OPSCC was strongly associated with the presence of HPV16 E6- and/or E7-reactive tumor-specific CD4$^+$ and CD8$^+$ TILs [2], which were detected in 57% of the HPV16$^+$ OPSCC patients. The dichotomy of HPV16-induced OPSCC with or without the presence of tumor-specific TILs provides an exceptional opportunity to identify TIME features associated with immune responsiveness (IR$^+$) or lack thereof (IR$^-$) using a multi-modal high-dimensional approach. Our studies in treatment naive tumor tissues revealed distinct interactions of CD8$^+$ and CD4$^+$ T cells with different myeloid cells between HPV16$^+$IR$^+$ and HPV16$^+$IR$^-$ OPSCC patients. These differences were associated with higher expression of *CXCL12* and *LTB,* as well as the clonal expansion of T cells producing CCL4 in HPV16$^+$IR$^+$ OPSCC compared to its IR$^-$ counterpart. Clinical and bulk mRNA sequencing data from The Cancer Genome Atlas (TCGA) [11] confirmed our findings in an independent HPV16$^+$ OPSCC cohort.

Materials and methods

Patients

Patients included in this study were part of a larger prospective observational study in OPSCC. Patients with histologically confirmed OPSCC were included in the P07-112 study investigating the circulating and local immune response in patients with head and neck cancer.[2 12] Patients were included after signing informed consent. The study was in accordance with the Declaration of Helsinki, and approved by the local medical ethical committee of the Leiden University Medical Center (LUMC) and in agreement with Dutch law. All the tumor material investigated in this study was obtained prior to therapy. Patients were treated with standard of care therapy consisting of surgery, radiotherapy, chemotherapy or combinations thereof. HPV typing on formalin-fixed paraffin-embedded (FFPE) tumor sections was performed as described.[2 12] Tumor staging was performed according to the National Comprehensive Cancer Network (https://www.nccn.org/professionals). An overview of the study design is shown in **Supplemental Figure 1A**. A summary of the OPSCC patient characteristics and performed tumor analyses is provided in **Supplemental Table 1**. The overall survival (OS) of the patients was updated until February 2021.

Blood and tumor cell isolation

Venous blood samples (54ml) were drawn in sodium heparin tubes (BD Bioscience) prior to surgery and processed within 6 hours. Peripheral blood mononuclear cells (PBMC) were isolated using Ficoll density centrifugation and stored in the vapor phase of liquid nitrogen until use. Tumor material was obtained from the operation theater or from the outpatient clinic. One part of the tumor was fixed in formalin and embedded in paraffin for routine diagnostics at the pathology department, whereas the other part was used in parallel for single-cell dissociation and culture of tumor infiltrating lymphocytes (TIL), as described.[2 12] In brief, OPSCC tumors were cut into small pieces. One third of the tumor pieces were put in culture in IMDM supplemented with 10% human AB serum (Capricorn Scientific, Ebsdorfergrund, Germany), 100IU/ml penicillin, 100µg/ml streptomycin, 2mM L-glutamine (Lonza, Breda, Netherlands; IMDM complete) and 1000IU/ml human recombinant IL-2 (Aldesleukin, Novartis, Arnhem, the Netherlands). Cultures were replenished every 2-3 days until sufficient cells were obtained. Two third of the tumor pieces was incubated for 15 minutes at 37°C in IMDM dissociation mixture containing 10% human AB serum, high dose of antibiotics (as above) and 0.38mg/ml Liberase (Roche Liberase TL research grade, Sigma Aldrich Chemie N.V., Zwijndrecht, the Netherlands). Following incubation, the cell suspension was passed through a 70µm cell strainer (Falcon, Durham, NC, USA) to obtain a single-cell suspension, counted using trypan blue exclusion (Sigma Aldrich Chemie N.V.), and cryopreserved at approximately 2 million cells/vial. All cells were stored in the vapor phase of liquid nitrogen until further use.

Tumor-specific T cell reactivity analysis

Cultured TIL batches were analyzed for the presence of HPV16-specific T cells as described previously.[2] To this end, reactivity of the cultured TIL was tested using autologous monocytes loaded with 5µg/ml HPV16 E6/E7 synthetic long peptides (SLP; 22-mers with 14 amino acids overlap) in a 5-day [3H]-thymidine-based proliferation and cytokine production assay. PHA (0.5µg/ml, HA16 Remel, Thermo Fisher Scientific, Bleiswijk, the Netherlands) served as a positive control, while unloaded monocytes served as negative controls. At day 1.5 and 4, supernatant (50µl/well) was harvested for cytokine analyses. Antigen-specific IFNγ, TNFα, IL-10 and IL-5 production was measured by using a cytometric bead array (CBA, Th1/Th2 kit, BD Bioscience, Breda, the Netherlands). The cut-off value for cytokine production was 20pg/ml, except for IFNγ for which it was 100pg/ml. Antigen-specific CCL4 and CXCL13 production was assessed by a custom-made 2-plex cytokine assay (Luminex; ProcartaPlex Immunoassay, Thermo Fisher

Scientific). Positive cytokine production was defined as at least twice above that of the unstimulated cells. HPV16 reactivity was also determined by intracellular cytokine staining (ICS). ICS was performed with antibodies for the markers CD3, CD4, CD8, CD137, CD154, IFNγ, TNFα and CCL4 following stimulation with HPV16 E6/E7 synthetic long peptide-loaded EBV-transformed B-lymphoblastoid cell lines (BLCL) as described.[12] Unloaded BLCL served as negative control and PHA as positive control. A positive response was defined as at least two times the value of the negative control, and at least 10 events in the gate. Acquisition was done on a LSRII Fortessa (BD Biosciences, LUMC flow cytometer core facility) and data analysis with FlowJo software (version 10.7.1).

NanoString PanCancer IO360 panel analysis

Archived diagnostic FFPE histological specimens were used to cut ten consecutive sections of 10μm for RNA extraction. Directly before and after these 10μm thick sections, a 4μm section was cut for hematoxylin-eosin (HE) staining. An OPSCC-specialized pathologist annotated tumor regions on these two HE slides to ensure that all 10μm slides contained tumor. After the sections were deparaffinized, the tumor areas were macro-dissected using the annotated HE slides as reference and placed in Buffer PKD of the RNA FFPE isolation kit (Qiagen, Hilden, Germany). RNA was isolated according to the manufacturer's instruction. The quality and quantity of the RNA was verified with the Agilent 2100 Bioanalyzer System, making use of the RNA 6000 Nano kit (Agilent, Santa Clara, CA, USA). Samples were selected for further processing when >15% of the RNA fragments were >300bp and the corrected RNA concentration remained ≥60μg/μl. To measure the gene expression profiles, 300ng of RNA from each sample was hybridized with the probes of the human PanCancer IO360 panel for 17 hours at 65°C, following the manufacturer's instructions (NanoString Technologies Inc., Seattle, WA, USA). The number of copies of each gene in every sample was counted by scanning 490 Field Of View using the nCounter® MAX system (NanoString Technologies). The raw data (counts of genes) were uploaded to the nSolver™ 4.0 software (NanoString Technologies), after which a quality check was performed in the gene expression analysis. The 20 housekeeping genes in the IO360 panel facilitated sample-to-sample normalization. Eight negative controls and six synthetic positive controls were included. The data were reviewed for reliability and validity based on the imaging (>0.75) and binding density (0.1-2.25) quality control metrics, and performance check of the positive controls (0.95-1). Samples with less than 8 housekeeping genes with >100 counts were removed during quality control (n=3). The data were analyzed using nCounter Advanced Analysis module 2.0 software (NanoString Technologies), in which automated cell type profiling and

pathway analysis based on the expression of pre-defined genes was performed (**Supplemental Table 2**). Benjamini-Hochberg adjusted *P*-values were used to decrease the false-discovery rate. Differentially expressed genes (DEGs) were defined by a log2 fold difference of >1 or ≤1 and an adjusted *P*-value<0.05.

Imaging mass cytometry and imaging processing analysis pipeline

Imaging mass cytometry (IMC) was performed using a previously optimized 33-marker panel.[13] FFPE whole tumor sections of 4μm thick were deparaffinized. Heat induced epitope retrieval was performed with citrate (10mM, pH6.0), and SuperBlock (Thermo Fisher Scientific) was used to block nonspecific binding sites. The first mix of 16 heavy metal conjugated antibodies was incubated for 5 hours at room temperature, the second mix of 17 heavy metal conjugated antibodies was incubated overnight at 4°C. Finally, an intercalator (DNA binder) was applied. An overview of the antibodies and their conjugated heavy metals can be found in **Supplemental Table 3**. The tissue slides were then analyzed by IMC using the Hyperion system (Fluidigm). Tumor regions were annotated by a pathologist, and two to three 1mm^2 regions per tumor were analyzed to account for intra-tumoral heterogeneity. The selected regions on the slides were laser ablated and processed through a mass cytometer, after which the detected heavy metals and their corresponding antibody (marker) were linked to the ablated region with a sub-cellular resolution of 1μm^2 per pixel (overview IMC workflow provided in **Supplemental Figure 1BC**).

The generated high-dimensional output was analyzed with a newly developed imaging processing pipeline, combining multiple previously validated publicly available software programs. The pipeline incorporates 6 automated consecutive steps, of which an overview is presented in **Supplemental Figure 1C**. Firstly, the signal of the markers were normalized, to prevent sample biased clustering as this is frequently encountered when using FFPE tissue. Semi-supervised machine learning was employed to train the software to distinguish signal from background noise for each individual marker, using the software programs Ilastik and CellProfiler [14], creating a binarized mask in which markers with their location on the image were expressed. Secondly, the same semi-supervised machine learning approach was used to segment the tissue into tumor and stroma, as well as to segment the individual cells on the images. These masks with layers of required information (normalized signal for all 33 markers, tissue segmentation, cell segmentation) were then combined in a single FCS file using ImaCyte (in-house developed software program for IMC data analysis, https://github.com/biovault/ImaCytE).[15] HSNE-based cell clustering was performed with Cytosplore

[16], and cluster verification and phenotype calling was performed using MCD Viewer and ImaCyte. After these pre-processing steps, quantitative analysis of the identified clusters was performed using ImaCyte. Spatial high-dimensional cell-cell interaction analyses and cellular microaggregate detection (more than three cells directly neighboring each other) were performed using ImaCyte and R. Permutation testing with 1000 iterations was performed to identify spatial interactions that occurred more frequently than expected based on chance, thus correcting for the cell cluster frequency. Only interactions with a permutation based Z-score>2 (i.e. outside 95% normal distribution range) were included for further analyses. To study differences in spatial interactions across two subgroups ($HPV16^{+}IR^{-}$ versus $HPV16^{+}IR^{+}$), interactions with a permutation based Z-score>2, occurring at a frequency of at least 2 fold more in either of the subgroups were included in the comparative analyses.

Single-cell RNA sequencing and data analysis

Single-cell tumor samples were thawed and enriched for viable $CD3^{+}$ T cells and $CD56^{+}$ NK cells using the dead cell removal kit (Miltenyi Biotec), followed by combined CD3/CD56 microbeads-guided magnetic cell enrichment (Miltenyi Biotec) according to the manufacturer's instructions. After isolation viability was more than 70% and percentage CD3/CD56 was 62.5 (range 27.5-97) and percentage B cells was 28.7 (range 1.6-64.8). Single-cell RNA sequencing (scRNAseq) was performed as we described previously.[17] In brief, between 2,108 and 6,107 sorted cells per sample were loaded on a Chromium Single Cell Controller (10x Genomics), lysed and barcoded. Reverse transcription of poly-adenylated mRNA from single-cells was performed inside each gel bead emulsion using the Single Cell 5'gene expression library workflow. Next-generation sequencing libraries were prepared in a single bulk reaction, and transcripts were sequenced using the HiSeq4000 System (Illumina). FASTQ files were pre-processed with cell ranger v3.0.0 (10x Genomics) using the GRCh38 reference genome. Quality control and downstream analysis was performed using Scanpy v1.6.0 [18] and Scirpy v0.6.1 [19]. All scripts used to perform the analysis are combined in one fully reproducible Nextflow pipeline and publicly available from GitHub (https://github.com/icbi-lab/abdulrahman2021_paper). Briefly, low quality cells were excluded retaining only cells with I) >700 detected genes, II) > 2000 detected reads, and III) <11% mitochondrial reads. Cells with more than one TCR-β or more than two TCR-α chains were discarded as putative doublets, in addition to computational doublet detection using *SOLO*.[20] Ribosomal, mitochondrial and T-cell receptor genes were excluded from downstream transcriptomic analysis. Raw counts were normalized per cell and log-transformed. Finally, the 6000 most

highly-variable genes (HVGs) of 14,242 T cells and 2,820 NK cells were selected and used for unsupervised Leiden clustering.[21] Embeddings were visualized using UMAP.[22] Differential gene expression between clusters was computed using edgeR [23], including the number of detected genes into the linear model.

Statistical analysis

Statistical data analysis was performed with GraphPad Prism 8.0.1 (GraphPad Software Inc., LA Jolla, CA, USA), which was also used to create graphs to visualize the data. The median immune counts of the three different OPSCC subgroups (HPV^-, $HPV16^+IR^-$, $HPV16^+IR^+$) were compared with the non-parametric Kruskal Wallis test, of two subgroups ($HPV16^+IR^-$ versus $HPV16^+IR^+$) with the non-parametric Mann-Whitney U test. Spearman correlation was used to study correlations between the identified (super)clusters. Differences in survival, HR with 95% confidence interval, were calculated with the non-parametric Mantel-Cox test. Two-sided $P<0.05$ were marked as statistically significant.

Results

Differences in immune signature between OPSCC patient groups with different clinical outcomes.

The OS data from our prospective cohort of 128 OPSCC patients extended earlier observations [3] showing that patients with HPV^+ OPSCC displayed a better clinical outcome than HPV^- OPSCC. Importantly, the TILs of 35 out of 61 tested patients with $HPV16^+$ OPSCC displayed reactivity against the E6 and/or E7 viral oncoproteins (IR^+). The fate of this $HPV16^+IR^+$ patient group, of which >90% had at least 5 years of follow up, was much better as they displayed superior survival when compared to the $HPV16^+IR^-$ group (**Figure 1A**), providing a firm basis for a positive role of local T-cell immunity in OPSCC. Differences in survival based on anatomical tumor location could be excluded (**Supplemental Table 1**), and the influence of smoking, TNM stage and received therapy on survival was excluded earlier [2].

Differences in gene expression, both at pathway and individual gene levels, were studied in 21 OPSCC patients (n=8 HPV^-; n=6 $HPV16^+IR^-$; n=7 $HPV16^+IR^+$) using the NanoString human PanCancer IO360 panel, with a particular focus on immune-related pathways including estimation of immune cell abundance. This approach revealed 43 differentially expressed genes (DEGs) between $HPV16^+IR^+$ and $HPV16^+IR^-$ OPSCC patients (**Figure 1B, Supplemental Table 2A**). The immune profile of HPV^- and $HPV16^+IR^-$ OPSCC patients was highly similar as only one DEG was detected (**Supplemental Figure 2A, Supplemental Table 4B**), and 209 DEGs

were detected between HPV$^-$ and HPV16$^+$IR$^+$ OPSCC patients (**Supplemental Figure 2B, Supplemental Table 4C**). A number of the upregulated DEGs (P<0.05) in HPV16$^+$IR$^-$ OPSCC compared to HPV16$^+$IR$^+$ OPSCC are associated with suppressive myeloid cells (*CCL20, CXCL3, CSF2, TREM1, IL-1B*) [24], angiogenesis (*CXCL8)* [25], TGFβ pathway (*INHBA, BMP2*) [26] and immune suppression (*IL-11*) [27]. The top upregulated DEGs in HPV16$^+$IR$^+$ compared to its IR$^-$ counterpart were *BLK*, reflecting B cells (**Supplemental Figure 2C**), and the chemokines *LTB* and *CXCL12* that are involved in ectopic lymphoid structure development, required for the coordination of adaptive immune responses.[28] Interestingly, the well-known chemokines for T cell attraction CXCL9, CXCL10 and CXCL11 did not differ.

ClueGO analyses of all DEGs between the two HPV16$^+$ patient groups [29] indicated a strong relation with immune enrichment processes related to IFNγ signaling, T cell activation, T cell receptor signaling, and mononuclear cell differentiation in HPV16$^+$IR$^+$ tumors (**Figure 1C**). Gene expression-based cell type profiling (**Supplemental Table 2**) suggested an increased infiltration by immune cells in the HPV16$^+$IR$^+$ group, including T cells, CD8$^+$ T cells, natural killer (NK, CD56dim) cells, cytotoxic cells, and macrophages (**Figure 1D**). This group also displayed a stronger involvement of several immune signaling pathways, including antigen presentation, co-stimulatory signaling, IFN signaling, cytokine and chemokine pathway, cytotoxicity, apoptosis, cell adhesion and migration pathway (**Figure 1E**).

Assessment of the impact of the three top upregulated DEGs in HPV16$^+$IR$^+$ and HPV16$^+$IR$^-$ on survival revealed that higher expression of *BLK*, *LTB* and *CXCL12* was associated with longer OS, in our own discovery cohort as well as in in a larger independent group of 69 patients with HPV16$^+$ OPSCC from the publicly available The Cancer Genome Atlas (TCGA) database [11] (**Figure 1F, Supplemental Figure 2D**), whereas there was no clinical impact for the three top upregulated DEGs in HPV16$^+$IR$^-$ (**Supplemental Figure 2E**). Specifically *LTB* expression was consistently related to the presence of CD4$^+$ T cells, CD8$^+$ T cells, CD11c$^+$ myeloid (*ITGAX*) cells and the expression of Tbet (*TBX21*) (**Figure 1G, Supplemental Figure 2F**). Furthermore, *LTB* expression was strongly related to genes of immune cell activation *(RELA, NFKB1, NFKB2, TNF)* but not with *RELB* and *MET* **Supplemental Figure 2G**), previously reported in the context of LTB to be associated with migration of tumor cells.[30]

Overall these data suggest that the OPSCC of HPV16$^+$IR$^+$ patients displays a hot immune signature with a chemokine-driven coordinated influx of different immune cells, whereas HPV16$^+$IR$^-$ OPSCC display upregulation of genes related to poor survival. These data fit well with the clinical fate of these groups, showing a long OS for HPV16$^+$IR$^+$ and shorter OS for HPV16$^+$IR$^-$ and HPV$^-$ OPSCC patients.

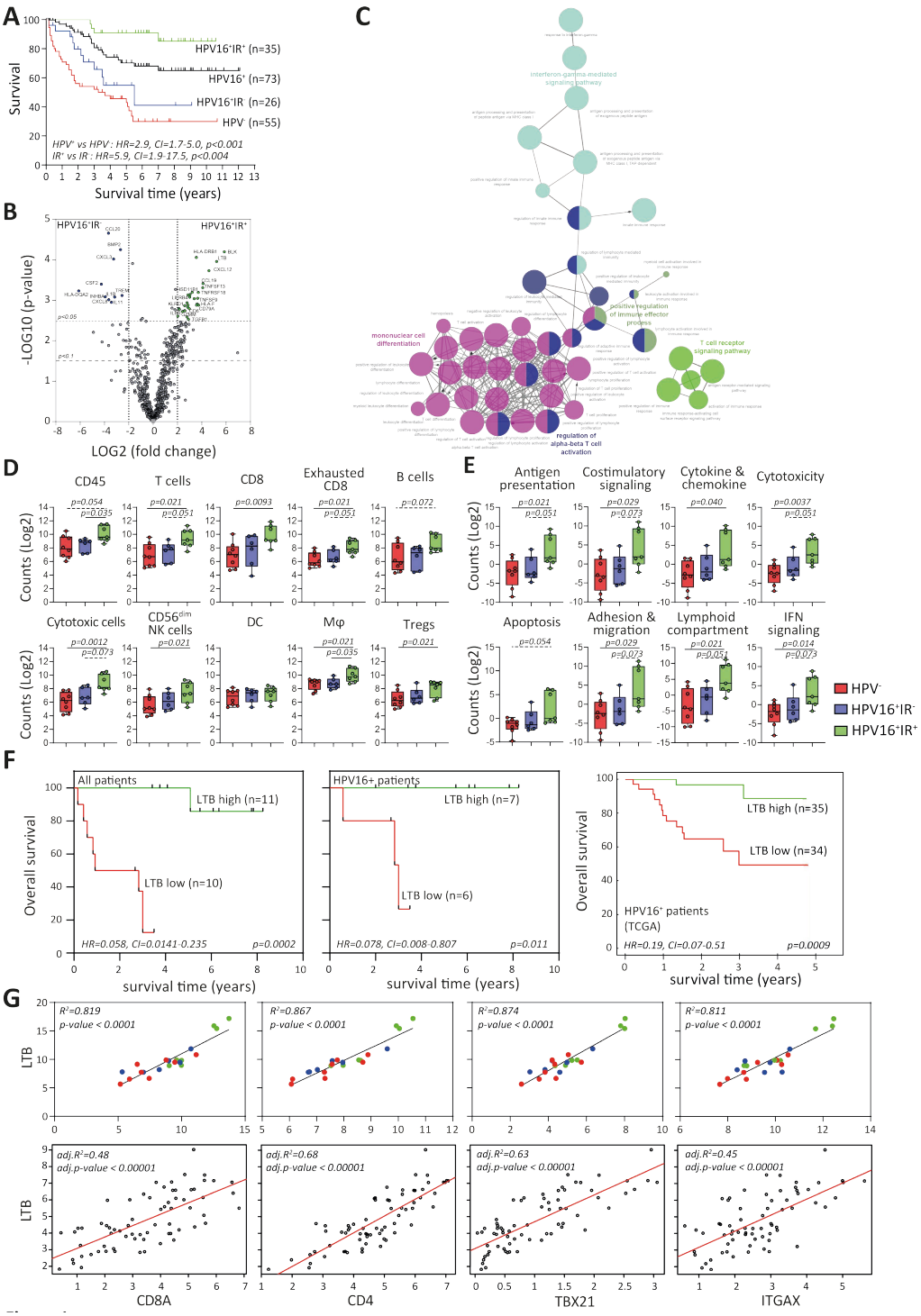

Figure 1. Immune signature of TME impacts survival of OPSCC patients.

***A**) Kaplan-Meier survival curves of prospectively followed cohort of HPV⁻ and HPV16⁺ OPSCC patients, the latter who are also subdivided into those with a tumor-specific T cell response (HPV16⁺IR⁺), and those lacking this immune response (HPV16⁺IR⁻). **B**) Volcano plots of upregulated DEGs identified by NanoString Pancancer IO360 between HPV16⁺IR⁺ (right) and HPV16⁺IR⁻(left). The dotted lines indicate the Benjamini-Hochberg adjusted P<0.05 and P<0.1 thresholds. **C**) ClueGo of DEGs (P<0.1) between HPV16⁺IR⁺ and HPV16⁺IR⁻ patients, visualizing the pathways in which these genes are involved. **D**) Deconvoluted cells by expression of genes predefined for different immune cell types depicted as counts in HPV⁻, HPV16⁺IR⁻ and HPV16⁺IR⁺ OPSCC. **E**) Differential expression of predefined pathway genes in HPV⁻, HPV16⁺IR⁻ and HPV16⁺IR⁺ OPSCC. **F**) Kaplan-Meier survival curves based on high/low LTB expression (classification based on median LTB expression), in all OPSCC patients analyzed by NanoString Pancancer IO360 (n=21), in the HPV16⁺ patients within this cohort (n=13), and in a large independent TCGA cohort of HPV16⁺ OPSCC (n=69). **G**) Linear regression analyses of top upregulated DEG LTB in HPV16⁺IR⁺ compared to HPV16⁺IR⁻ OPSCC versus cell type profiles of CD8 (CD8A), CD4, Tbet⁺ T cells (TBX21) and DC (ITGAX, CD11c) both for this cohort (n=21, upper panel) and the TCGA cohort of HPV16⁺ OPSCC (n=69, lower panel). HPV⁻ (red), HPV16⁺IR⁻ (blue) and HPV16⁺IR⁺ (green).*

Identification and quantification of 51 different cell clusters in the TME of OPSCC.

To provide a detailed inventory of the *in situ* immune landscape of OPSCC we extensively characterized the tumors of 20 patients (n=5 HPV⁻; n=4 HPV16⁺IR⁻; n=11 HPV16⁺IR⁺) using a previously optimized 33-marker panel for imaging mass cytometry [13], and an imaging processing pipeline (**Supplemental Figure 1C**). A total of 142,868 tumor cells, 46,907 stromal cells and 274,775 immune cells (**Supplemental Figure 1D**), were identified in the images (**Figure 2A**) for cluster quantification and for spatial and cell interaction analyses. These cells formed 51 clusters, comprising 14 tumor, 15 lymphoid, 15 myeloid, and 7 other cell clusters (**Supplemental Figure 3A**), all of which were verified in the raw images using MCD Viewer (**Supplemental Figure 4**). The 51 clusters (c) were then grouped into 18 mutually exclusive superclusters (sc) (**Supplemental Figure 3A**), and in 10 non-mutually exclusive superclusters, based on the expression of a particular lineage marker of interest expressed by multiple clusters (**Supplemental Table 5**).

Quantification of the 51 cell clusters (**Supplemental Figure 5**) and 18 mutually exclusive superclusters immediately revealed differences in tumor composition between the three OPSCC groups studied. The HPV16⁺IR⁺ tumors displayed the highest percentage of immune cells among all counted cells in the TME (**Figure 2B**). They were richer infiltrated by T cells, M1 macrophages and dendritic cells (DCs) (**Figure 2BC, Supplemental Figure 3B**). The OPSCC of HPV16⁺IR⁻ and HPV⁻ patients contained relatively more tumor cells, fibroblasts and blood vessels, indicative for a more tumor-promoting environment. The HPV⁻ OPSCC contained the lowest percentage of immune cells (**Figure 2BC, Supplemental Figure 3B**). The differences observed in the cellular composition of OPSCC among the three patient groups underline the transcriptomic signatures found by NanoString analyses and relate to their corresponding clinical course.

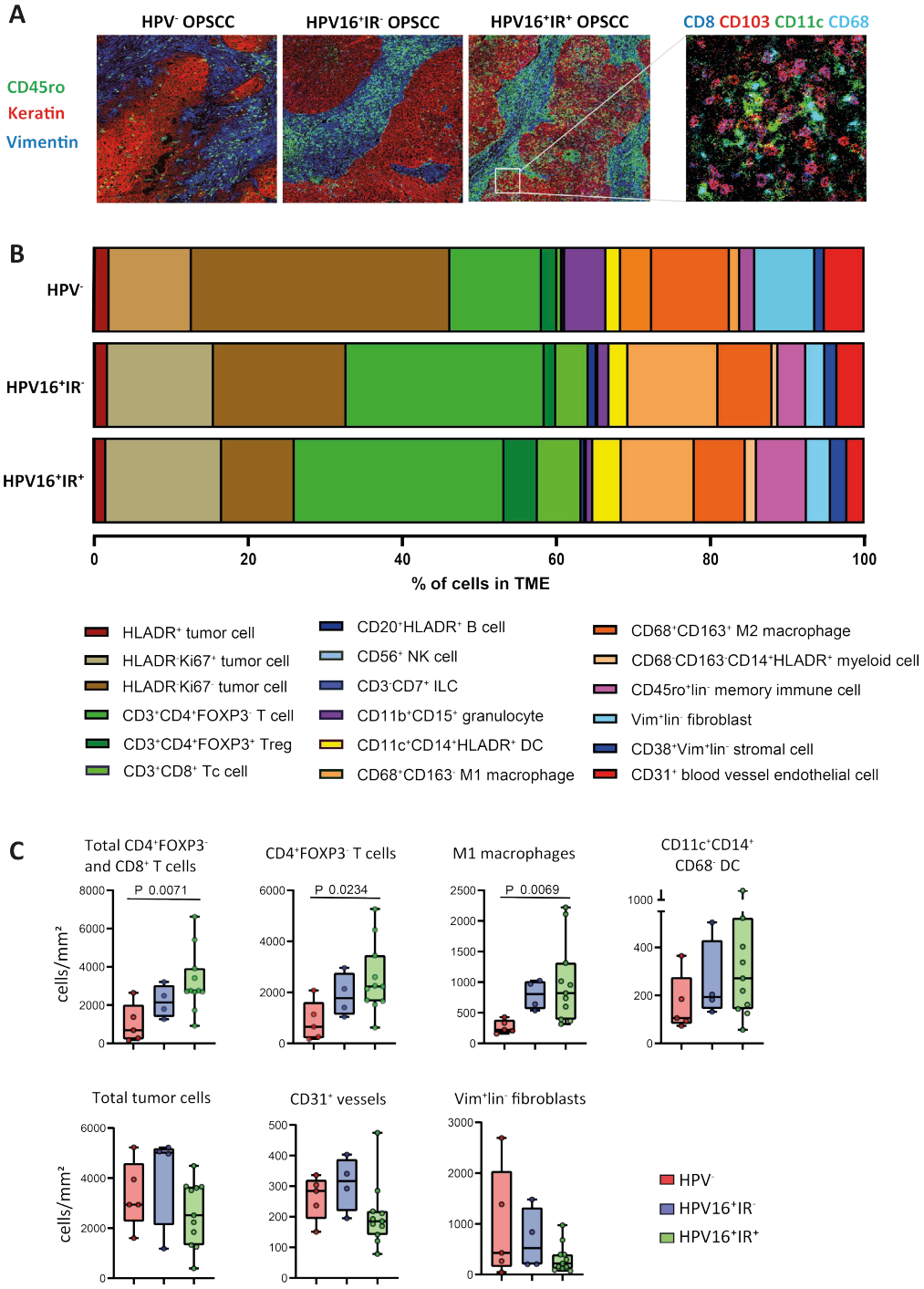

Figure 2. Imaging mass cytometry identifies cell clusters present in different percentages across OPSCC subgroups.

***A**) Representative images of immune cell infiltrate in the context of the microenvironment of OPSCC, as found in the three distinct subgroups (HPV$^-$, HPV16$^+$IR$^-$, HPV16$^+$IR$^+$), visualizing the spatial location of immune cells (CD45ro in green) in the tumor epithelium (keratin in red) and stroma (vimentin in blue) region. A selection of both lymphoid and myeloid cell markers in the same image is also shown.*
***B**) Fractional composition of the TME of the three OPSCC subgroups, depicting the median percentage of the 18 superclusters. **C**) Boxplots visualizing the quantitative cell counts in the whole tumor of the most differential superclusters across the three OPSCC subgroups: HPV$^-$ red (n=5), HPV16$^+$IR$^-$ blue (n=4) and HPV16$^+$IR$^+$ green (n=11).*

Principally different immune cell interactions in HPV16$^+$IR$^+$ versus HPV16$^+$IR$^-$ patients.

Immune-mediated tumor control requires a coordinated response of several immune cell types in a spatial and dynamic manner.[31] Spearman correlation heatmaps generated for the 28 superclusters revealed strong positive and negative correlations between the counts of various cell types in HPV16$^+$IR$^+$ tumors (**Figure 3AB**). Linear regression analyses for those phenotypes with a correlation coefficient >0.6 and P<0.01 were analyzed, showing in particular strong associations between the counts of (CD103$^+$) CD8$^+$ T cells with DCs and with CD14$^+$ inflammatory myeloid cells in HPV16$^+$IR$^+$ patients (**Figure 3BC**). No significant correlations were detected in HPV16$^+$IR$^-$ OPSCC (**Supplemental Figure 6A**), emphasizing the lack of uniform immune cell organization in these tumors.

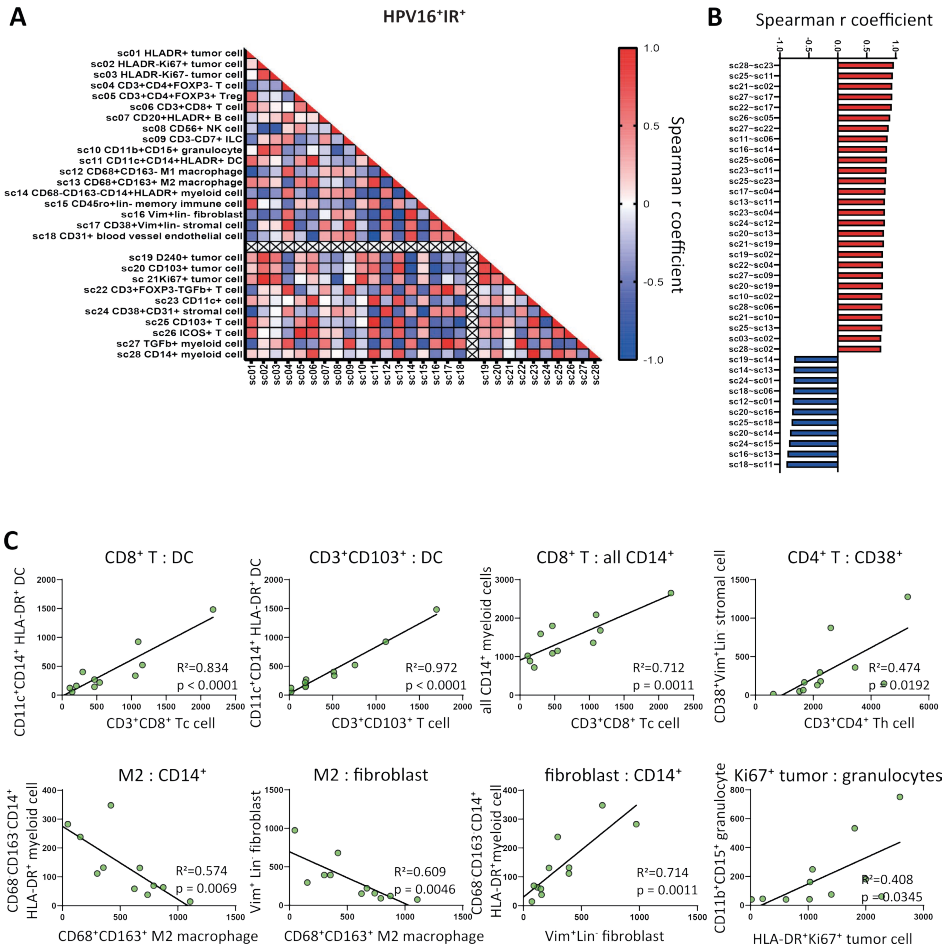

Figure 3. A coordinated and diverse immune infiltrate in HPV16⁺IR⁺ patients.

***A**) Spearman quantitative correlation heatmaps of the 28 superclusters (18 mutually exclusive, and 10 non-mutually exclusive) in the whole tumor in HPV16⁺IR⁺ OPSCC (n=11). The empty line separates mutually exclusive superclusters (above the crossed line) from the non-mutually exclusive superclusters (below the crossed line). **B**) Waterfall plot of statistically significant (P<0.01) Spearman correlations between the 28 superclusters (sc, defined in Supplemental Table 5) in HPV16⁺IR⁺ OPSCC (n=11), bars indicating their corresponding Spearman r coefficient. **C**) Linear regression analyses of the mutually exclusive superclusters with statistically significant (P<0.01) Spearman correlations in HPV16⁺IR⁺ OPSCC (n=11), including corresponding R squared values and linear regression P-values.*

The imaging mass cytometry data enabled us to study which cells are in close vicinity and, therefore, able to interact with each other at the single-cell level. Analysis of the 51 identified cell clusters revealed interactions between immune cells, tumor cells and other cells (**Figure 4A**). As expected [32] most cells sojourn in the neighborhood of cells from the same cluster (**Figure 4A**). A clear distinct

spatial phenotypic signature (SPS) became evident when only the interactions specifically occurring at a frequency that a) is higher than would be expected by chance, thereby correcting for differences in cell cluster frequencies by using permutation testing and b) is at least 2-fold higher in one of the subgroups, were visualized (**Figure 4B**). These spatial analyses revealed that in particular DCs and D2-40^{+} (invasive margin) tumor cells were more frequently interacting with both CD8^{+} T cells (c4) and CD4^{+} T cells (c14) in HPV16^{+}IR^{+} OPSCC (**Figure 4BC**). T cells (c4, c14) and CD14^{+}CD11c^{+}HLA-DR^{+}CD68^{-} DCs (c12, c13) formed simple immune cell aggregates [28] of more than three cells directly neighboring each other, designated as microaggregates, within the tumor cell beds of HPV16^{+}IR^{+} OPSCC (**Figure 4C**). Of note, these were not tertiary lymphoid-like structures, of which only one was found in one OPSCC image, and this image was excluded from further analysis as in OPSCC it cannot be differentiated from a normal germinal center. Flow cytometry on the tumor-infiltrating CD14^{+}CD11c^{+}HLA-DR^{+} cells revealed the co-expression of CD1c, CD32b, CD36, CD141, CD40 and CD86 (**Supplemental Figure 7**).

In HPV16^{+}IR^{-} OPSCC lymphocytes were found to interact with immunosuppressive myeloid cells, illustrated by interactions between NK cells (c8) and CD68^{+}CD204^{+}TGFβ^{+}CD14^{-} tumor associated M2 macrophages (c15) as well as CD14+CD204+ myeloid cells (c16), and interactions between CD4^{+}TGFβ^{+} T cells (c34) and CD14^{+}HLADR^{+}TGFβ^{+} myeloid cells (c17), or CD8^{+}CD103^{+} T cells (c8) with CD68^{+}CD163^{+} (c51) M2-like macrophages (**Figure 4B**). Notably, PD-L1 expression was not detected on these myeloid cells. The interactions between T cells and myeloid cells varied per patient in accordance with the earlier observed lack in coordination of immune cell infiltration in HPV16^{+}IR^{-} OPSCC. A 360° spatial composition analysis of DCs sustained the notion that these DC, CD8^{+} T cell, CD4^{+} T cell and tumor cell microaggregates are scarce in HPV16^{+}IR^{-} OPSCC (**Figure 4D**). Finally, visualization of the top 10 complete spatial immune compositions with highest Z-scores indicated dominant interactions with lymphocytes in HPV16^{+}IR^{+} OPSCC, while the TME in HPV16^{+}IR^{-} OPSCC was dominated by myeloid cell interactions (**Supplemental Figure 8**).

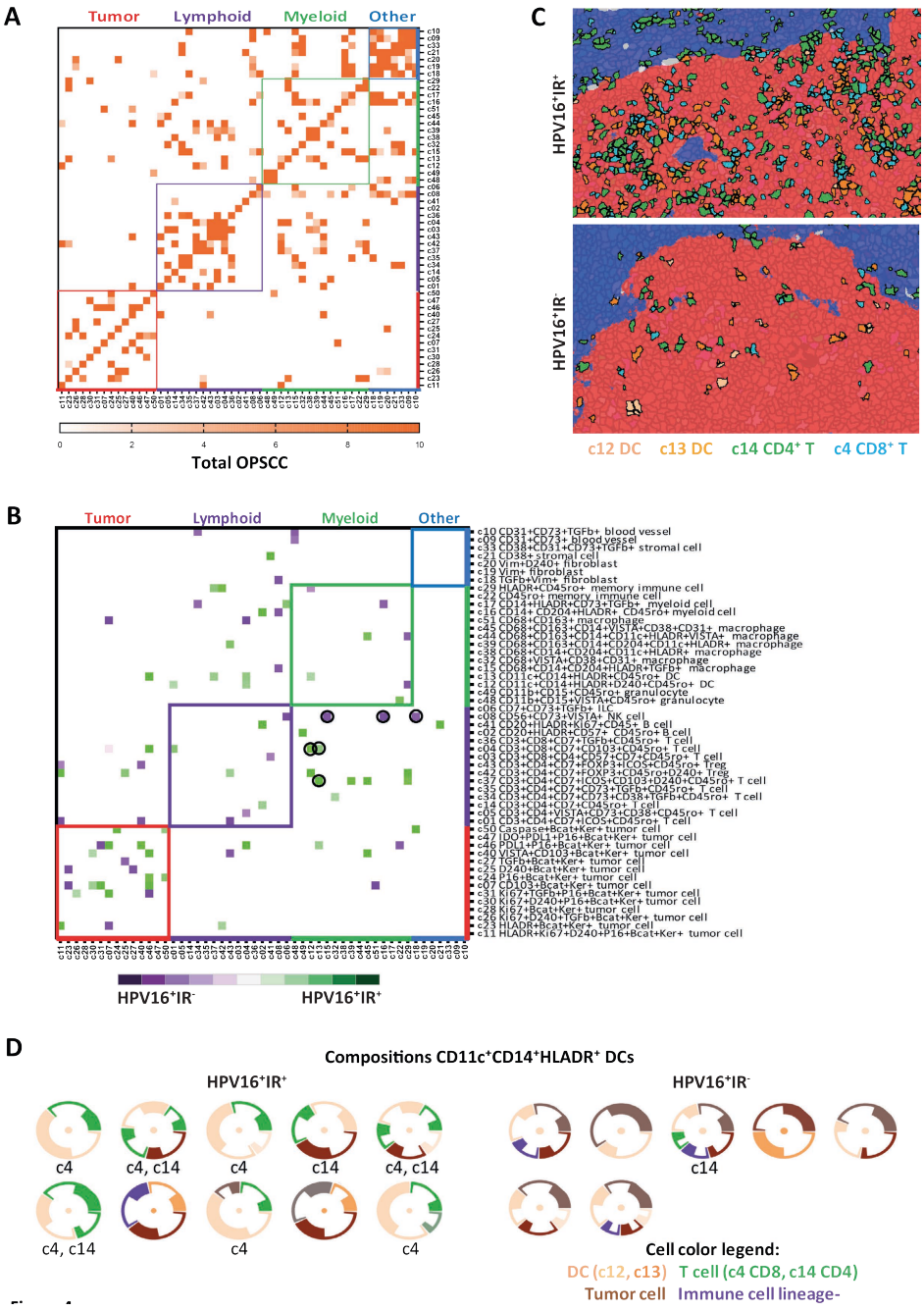

Figure 4. Organized intra-tumoral immune microaggregates specifically in HPV16^{+}IR^{+} OPSCC.

Spatial interactions heatmap of the 51 identified clusters (Supplemental Table 5), with interaction neighborhood defined as 5µm (<1 cell, direct spatial interaction). Cluster name is based on the markers that are expressed by that cluster, indicating that a cluster is negative for all other tested markers. ***A****) Spatial interactions heatmap of the total OPSCC cohort (n=20), showing all spatial interactions with a permutation verified Z-score>2 (i.e. outside the 95% normal distribution range), dark orange indicating highest Z-scores.* ***B****) Heatmap showing the differences in spatial interactions occurring in HPV16$^+$IR$^+$ (n=11) versus HPV16$^+$IR$^-$ (n=4) OPSCC. Only spatial interactions with a permutation verified Z-score>2, which specifically occurred in only one of the subgroups, and had at least a two-fold interaction difference in percentage between the subgroups are visualized. Spatial interactions occurring more frequently in HPV16$^+$IR$^+$ tumors are indicated in green, and in HPV16$^+$IR$^-$ tumors in purple.* ***C****) Hyperion images of the TME of OPSCC, showing the direct spatial interactions between CD8+ T cells, CD4+FoxP3- T cells and dendritic cells with tumor cells in HPV16$^+$IR$^+$ OPSCC, and the absence of these microaggregates in HPV16$^+$IR$^-$ OPSCC. Tumor epithelium is visualized in red, tumor stroma in blue.* ***D****) 360° spatial interaction compositions of DCs, for HPV16$^+$IR$^+$ and HPV16$^+$IR$^-$ tumors. Visualized is the DC (center), surrounded by other clusters (thin circle segment indicates standard deviation). Below each composition the involved T cell cluster numbers are given. Threshold for the 360° compositions: ≥20 occurrences.*

HPV16$^+$IR$^+$ patients show preferential T cell expansion in CD8$^+$ T cell clusters defined by the expression of CCL4.

The profound differences in spatial interactions of T cells and myeloid cells observed between HPV16$^+$IR$^+$ and HPV16$^+$IR$^-$ OPSCC is likely to bear impact on the function and phenotype of T cells present in these tumors. This was investigated by a combined single-cell transcriptome (scRNAseq) and T cell receptor (TCR) sequencing analysis on magnetic bead-sorted CD3$^+$ and CD56$^+$ cells from 13 patients (3 HPV$^-$, 4 HPV16$^+$IR$^-$, 6 HPV16$^+$IR$^+$), yielding data for 14,242 T cells and 2,820 NK cells. Unsupervised clustering [21] resulted in the detection of 32 T-cell clusters, comprising twelve CD8$^+$, eleven CD4$^+$, six FoxP3$^+$ (Treg) and three other CD3$^+$CD4$^-$CD8$^-$ T-cell (Tother) clusters, as well as six NK cell clusters (**Figure 5A**). All clusters were found in >1 patient (**Figure 5B and Supplemental Table 6**). Analysis of the distribution of these 38 cell clusters among the three OPSCC groups revealed a significant enrichment of clusters CD8_0 and Treg_0 in HPV16$^+$IR$^+$ when compared to HPV16$^+$IR$^-$ OPSCC (**Figure 5CDE and Supplemental Figure 9**). Top 30 DEGs of all clusters are listed in **Supplemental Table 7**.

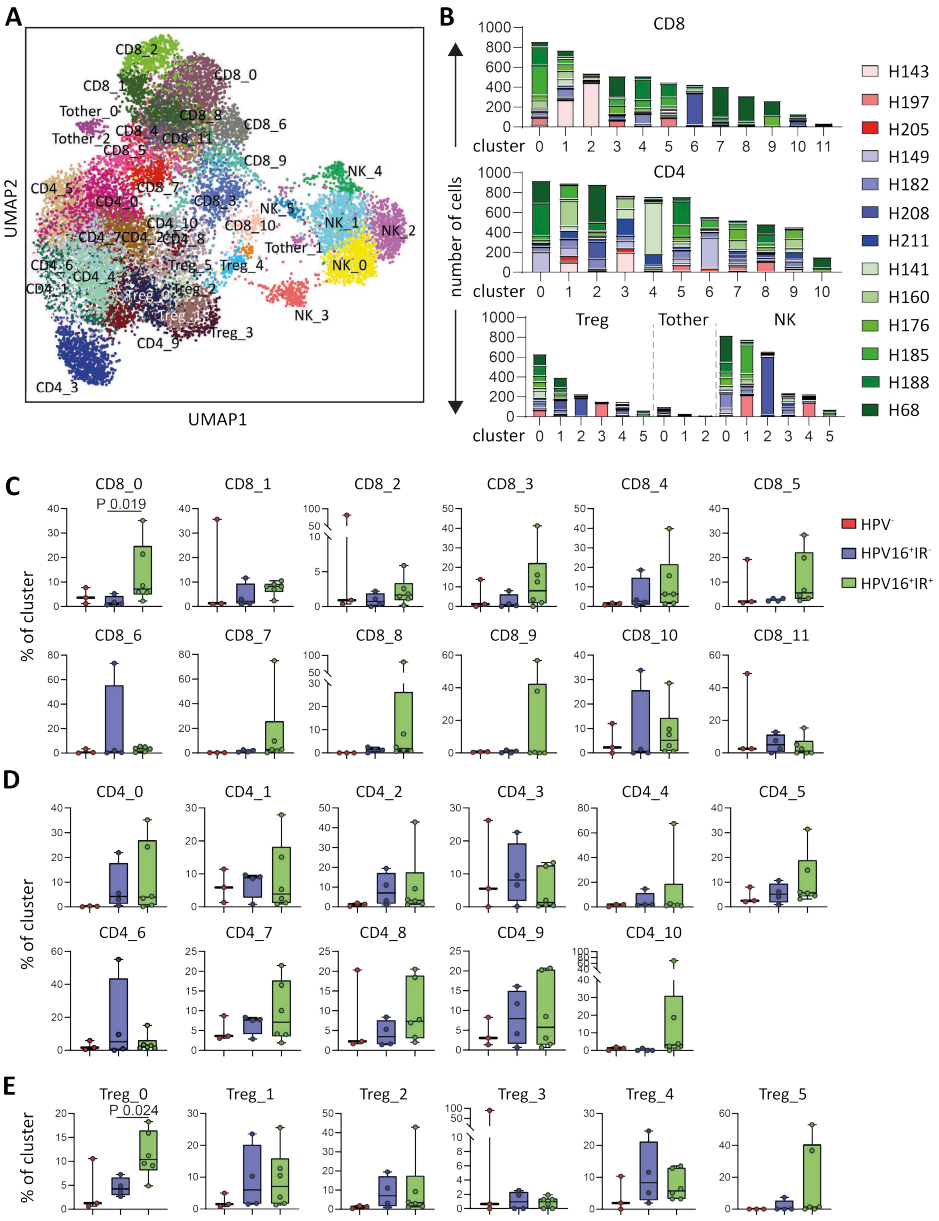

Figure 5. HPV16⁺IR⁺ patients show enrichment of clusters CD8_0 and Treg_0.

*Integrated single-cell transcriptome and TCR repertoire RNA sequencing analysis was performed on magnetic-bead sorted CD3⁺ T cells and CD56⁺ NK cells from 13 OPSCC samples. Following quality control and doublet-filtering, the 6000 most highly variable genes (HVG) of 14,242 T cells and 2,820 NK cells were selected and unsupervised clustering was performed using the Leiden algorithm [21]. **A**) A 2-dimensional UMAP plot visualizing the 38 identified clusters. **B**) Bar graphs depicting the number of cells per patient per cluster for CD8⁺ (top), CD4⁺ (middle) T cells and FoxP3⁺ T cells (Treg), Tother and NK cells (bottom; from left to right). **C**, **D**, **E**) Box plots depicting the identified CD8 (C), CD4 (D) and Treg (E) clusters, among HPV⁻ (red, n=3), HPV16⁺IR⁻ (blue, n=4) and HPV16⁺IR⁺ (green, n=6) OPSCC tumors. Data is represented as percentage of cluster.*

As the TCR is responsible for the specificity and intratumoral TCR clonal expansion may reflect tumor-reactivity [33], analysis of the TCR repertoire yields valuable information that can be connected to the IR status of the patients. Full-length TCR sequences were obtained for 75.4% of all T cells. In total 2,905 of the 10,734 cells (27.1%) were clonally expanded on the basis that at least 2 identical TCRs were found, resulting in a total of 690 of the 8,519 individual clonotypes (8.1%) being expanded. Clonotype network analysis revealed that clonally expanded TCRs are present in all patients and clonal expansion was the strongest and more frequent among $CD8^+$ T cells (**Figure 6A, Supplemental Figure 10A**). Moreover, the number of cells and clonotypes with expanded TCRs tended to be higher in $HPV16^+IR^+$ OPSCC among $CD8^+$ and $CD4^+$ T cells, but not among Treg and Tother cells (**Figure 6B, Supplemental Figure 10B**).

To link the preferentially expanded $CD8^+$ and $CD4^+$ T cells in $HPV16^+IR^+$ OPSCC to transcriptional profiles, integration of the single-cell transcriptome and TCR repertoire data sets was performed. Strong $CD8^+$ T-cell expansion existed in the majority of patients and clusters, whereas expansion of $CD4^+$ T cells and Tregs were lower or absent in some patients and clusters (**Supplemental Figure 10CD**). Importantly, the percentage of expanded cluster CD8_0 T cells was clearly higher (P=0.057) in $HPV16^+IR^+$ OPSCC than in IR^- OPSCC (**Supplemental Figure 11ABC**). The CD8_0 cluster can be defined as a cytokine-producing $CD8^+$ T cell subset, in which particularly *CCL4* was highly expressed. This subset differs substantially from cluster CD8_3, which did not significantly differ between our patient groups and is made up of cells that, based on their DEG profile, resemble highly activated tumor-resident cytotoxic effector T cells (**Supplemental Figure 12, Supplemental Table 7**). *CCL4* was also expressed by NK cells (**Figure 6C and Supplemental Figure 13**), but as NK cells were >20 fold less abundant than T cells in these tumors (**Supplemental Figure 3B**), their contribution is much lower. The production of CCL4 prompted us to re-examine the expression of chemokine receptors in the NanoString data. This revealed that the expression of CCR5 (CCL4's receptor), CCR2 (CCL2's receptor), CXCR3 (CXCL9,10,11's receptor) and CXCR6 (CXCL16's receptor) but not CXCR2, CXCR4 and CX3CR1, CCR4, was increased in HPV16+IR+ tumors compared to HPV16+IR- tumors (**Figure 6D**). Of note, none of the T and NK cell clusters showed expression of *CXCL12,* whereas *LTB* was expressed by the majority of the $CD4^+$ T-cell clusters (**Figure 6C and Supplemental Figure 13**). Extensive characterization of all the T and NK cell clusters in terms of tissue-residency, co-stimulatory and co-inhibitory genes is provided in **Supplemental Figure 12**, showing that in contrast to cluster CD8_3, cluster CD8_0 has an overall low expression of immune checkpoints.

To confirm that CCL4 was predominantly produced by T cells in HPV16^{+}IR^{+} OPSCC, the supernatants of TIL cultures from HPV16^{+} OPSCC were analyzed for the production of CCL4 and as control CXCL13, as it is expressed by cluster CD8_3 T cells which did not differ between the patient groups. While a similar production of CXCL13 was found in the PHA-stimulated cultures of IR^{+} and IR^{-} patients, CCL4 production was almost exclusively found in HPV16^{+}IR^{+} OPSCC, with all nine cultures showing substantial production of CCL4 when stimulated with tumor antigen or PHA (**Figure 6EF, Supplemental Figure 14**). Subsequent flow cytometric analysis showed that all IFNγ-producing CD8^{+} T cells co-produced CCL4, whereas half of the IFNγ-producing CD4^{+} T cell population produced CCL4 when stimulated with cognate antigen or PHA (**Figure 6GH**).

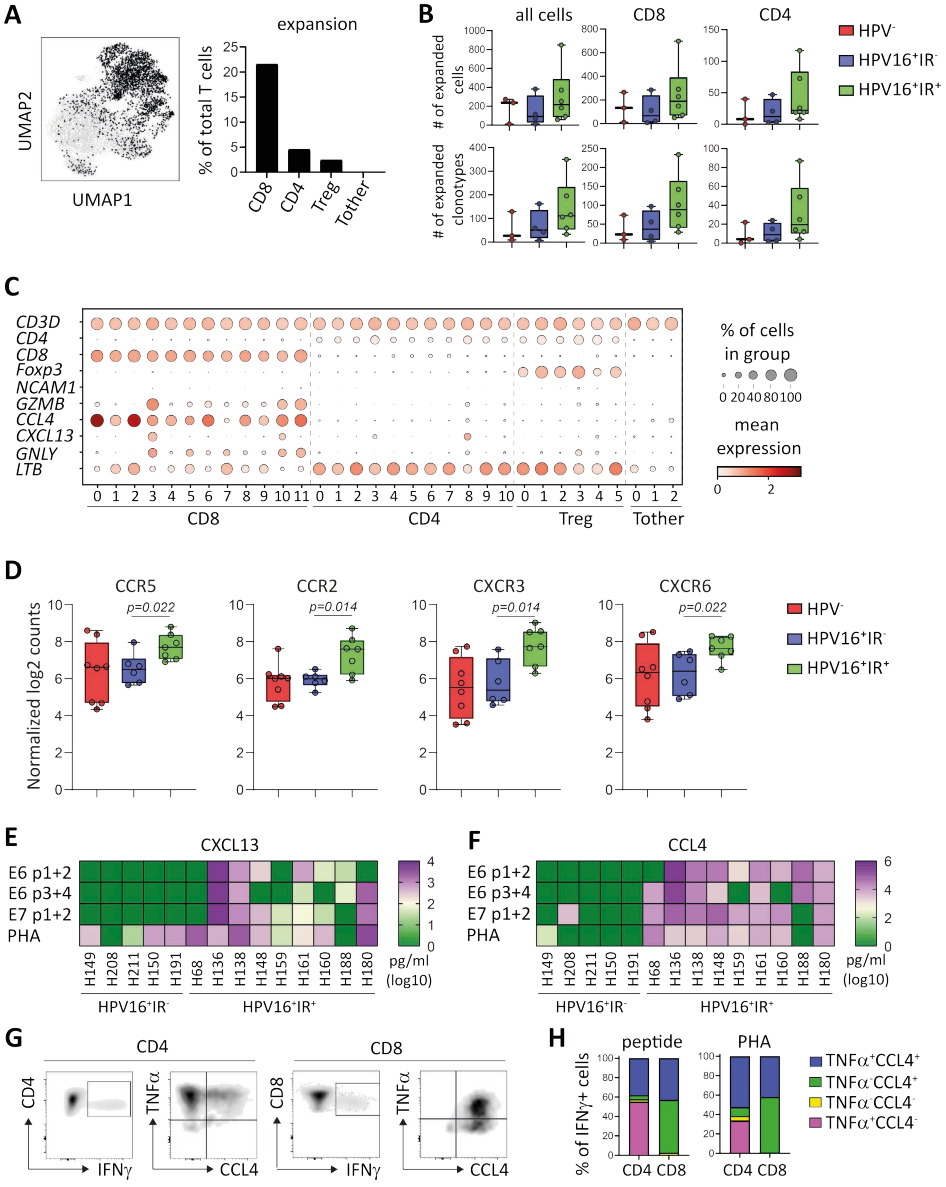

Figure 6. HPV16⁺IR⁺ patients show T cell expansion in clusters particularly defined by the expression of CCL4 or CXCL13.

*Integrated single-cell transcriptome and TCR repertoire RNA sequencing analysis was performed on magnetic-bead sorted CD3+ T cells and CD56+ NK cells from 13 OPSCC samples. **A**) UMAP plot depicting the localization of expanded TCR clonotypes (left) and graph depicting the percentage of expanded TCR clonotypes within CD8, CD4, Treg and Tother cells (right). **B**) Box plots displaying the number of expanded cells (top) and clonotypes (bottom) within all cells (left), CD8 (middle) and CD4 (right) cells detected in HPV⁻ (red, n=3), HPV16⁺IR⁻ (blue, n=4) and HPV16⁺IR⁺ (green, n=6) OPSCC patients. **C**) Dot plots showing the gene expression of selected determining genes in the clusters. **D**) Normalized log2 counts for the expression of chemokine receptors in HPV16⁺IR⁺ (green, n=7) compared to HPV16⁺IR⁻ (blue, n=6) OPSCC (Mann-Whitney*

*U test). **E**, **F**) Heatmap presenting specific (E) CXCL13 and (F) CCL4 cytokine production of cultured CD4⁺ and CD8⁺ T cell containing TIL in response to HPV16 E6 peptide (pool 1+2 and 3+4)-, HPV16 E7 peptide (pool 1+2)-loaded autologous monocytes for HPV16⁺IR⁺ (n=9) and HPV16⁺IR⁻ (n=5) OPSCC. PHA served as positive control. Three OPSCC TIL cultures containing HPV-specific T cells were analyzed for HPV16-specific cytokine production by intracellular cytokine staining and flow cytometry following stimulation with BLCL loaded with pools of HPV16 E6/E7 synthetic long peptides. Expression of CD3, CD4, CD8, IFNγ, TNFα and CCL4 following overnight stimulation in the presence of Brefeldin A. **G**) A representative example. The TIL were gated for viable and single cells, and further gated for CD3, CD4 and CD8. The cells producing TNFα and CCL4 within the CD8⁺IFNγ⁺ (left) and CD4⁺IFNγ⁺ (right) T-cell population are depicted. **H**) The percentage of TNFα and CCL4 within the total IFNγ-producing CD4⁺ and CD8⁺ T cells is depicted for two patients for HPV16 peptide (left) and three patients for PHA (right).*

CCL4 expression is related to T cell and DC tumor infiltration as well as survival in HPV16⁺ OPSCC TCGA patients.

Our T cell data indicated a role for CCL4 in a productive TIME, hence a gene set enrichment analysis of the TCGA RNA-sequencing data from the 69 patients with HPV16⁺ OPSCC [11] was performed. Our previously published immunogenomic analytic strategy to estimate subpopulations of tumor-infiltrating immune cells [34] was applied to determine which immune cells were relatively enriched or depleted in HPV16⁺ OPSCC with high versus low *CCL4* gene expression (**Figure 7A**). These analyses confirmed a positive relationship between *CCL4* with a larger fraction of activated and effector memory CD8⁺ T cells and activated CD4⁺ T cells as well as with B cells, T follicular helper cells, Tregs, macrophages and eosinophils suggestive for a more effective antitumor inflammatory response. This notion was supported by a strong correlation between the expression of *CCL4*, CD8⁺ T cells (*CD8A*), CD4⁺ T cells (*CD4*), Tbet⁺ T cells (*TBX21*) and CD11c⁺ myeloid cells (*ITGAX*) (**Figure 7B**) consistent with recent literature suggesting that CCL4 functions as a long-range homotypic signaling molecule to attract more T cells and cross-presenting DCs into the TME.[35 36]

To gain more information on the immune enrichment processes associated with high expression of *CCL4* in the tumor microenvironment, ClueGO analyses [29] were performed. This showed that especially *CCL4* was positively associated with T cell co-stimulation, activation, and proliferation as well as lymphocyte chemotaxis and IFNγ responses (**Figure 7C, Supplemental Figure 15**). Finally, the expression of *CCL4* was associated with superior disease control in patients with HPV16⁺ OPSCC (**Figure 7D**), indicating the significance of the immune response associated with this cytokine.

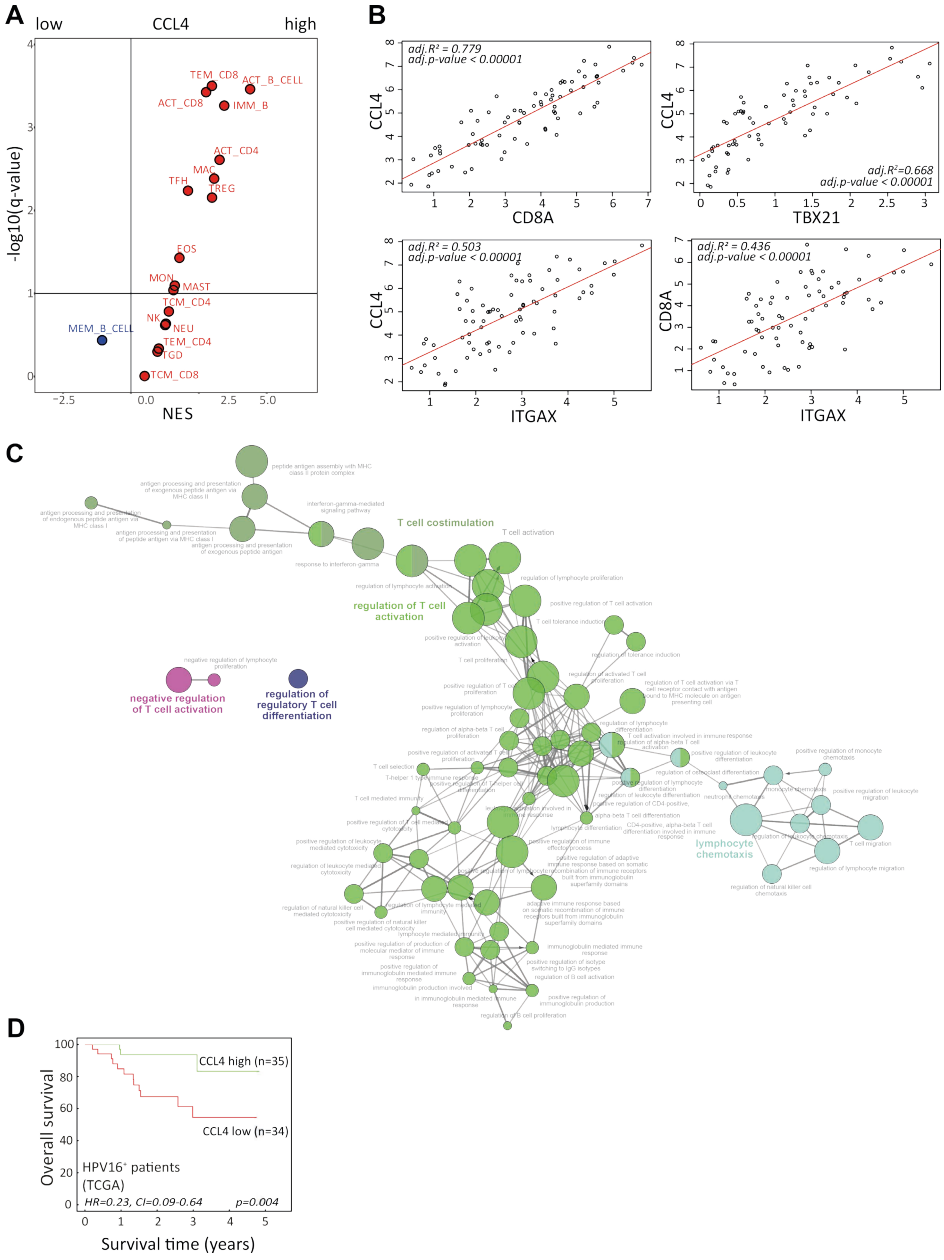

Figure 7. CCL4 associates with stronger antitumor immunity and improved survival.

***A**) To identify immune cell types that are overrepresented in HPV16-positive OPSCC with strong expression of CCL4, a gene set enrichment analysis was performed on a cohort of 69 patients with HPV16⁺ OPSCC present in the publicly available TCGA database. An average gene expression of each gene was calculated for a high and low group. The log2-fold change of expression level between groups was used as input for the GSEA pre-ranked analysis. The association was represented by a normalized enrichment score (NES). An immune cell type was considered enriched when the FDR (q-value) was <10%. The Volcano plot for the*

enrichment (red) and depletion (blue) of immune cell types in CCL4-high versus CCL4-low HPV16⁺ OPSCC is shown. ***B****) The Pearson correlation between the expression of CCL4 with CD8A (for CD8 T cells), TBX21 (for Tbet⁺ T cells) and ITGAX (CD11c for DCs) as well as CD8A and ITGAX in the tumors of the 69 patients with HPV16⁺ OPSCC in the TCGA database.* ***C****) The correlation between CCL4 with a subset of genes representing immune related functions selected based on correlation analysis (Pearson correlation coefficient (R) > 0.6; adjusted P<0.05) were used for gene ontology (GO) analysis of immune enrichment processes using ClueGO [29].* ***D****) Kaplan-Meier survival plots of the 69 patients with HPV16⁺ OPSCC in the TCGA database grouped according to high and low gene expression using the median value of CCL4 as cut-off.*

Discussion

This multi-modal high-dimensional study of the TIME in OPSCC revealed a distinct spatial phenotypic signature in the immune landscape of HPV16⁺IR⁺ and that of HPV16⁺IR⁻ OPSCC. Immune cell infiltration in HPV16⁺IR⁺ tumors is highly coordinated resulting in characteristic CD8⁺(CD103⁺) T cells, CD4⁺ T cells and DCs microaggregates within the tumor cell beds, a perfect place for DCs to ingest tumor antigens and stimulate tumor-specific T cells. In this study T cell:DC interactions are associated with longer OS but they have also been reported to be required for successful anti-PD1 therapy.[37] These microaggregates are most likely organized under the influence of the chemokines LTB and CXCL12 [28 38] and sustained by CCL4, known to attract T cells and cross-presenting DCs.[35 36 39] Indeed an increased expression of CCL4's receptor CCR5 was detected in HPV16⁺IR⁺ tumors compared to HPV16⁺IR⁻ tumors. Previously, it was shown that the production of CCL4 by tumor cells was key to attract DCs and to start tumor immunity.[9 36] Here we show that CCL4 can also be produced by tumor-specific T cells and lead to a productive TIME. While CCL4 is capable of attracting both tumor supporting (regulatory T cells, M2 macrophages, MDSC) and tumor-rejecting (cytotoxic T cells, M1 macrophages) immune cells, depending on the context in which it is produced [40], we did not observe differences in counts of regulatory T cells and macrophages, suggesting that in the HPV⁺IR⁺ context the chemotaxis of tumor-rejecting immune cells by CCL4 prevails.

The formation of organized aggregates by tissue infiltrating leukocytes occurs often during inflammation and such regions may exist as the simple aggregates found here inside the tumor cell bed, or as more sophisticated structures in the tumor stroma that resemble tertiary lymphoid structures (excluded in our imaging analyses) and are known to stimulate adaptive immunity.[28] Of the chemokines, LTB was produced by multiple CD4⁺ T-cell clusters, indicating that the sheer presence of more activated CD4⁺ T cells was responsible for its overexpression in HPV16⁺IR⁺ tumors. CCL4 was expressed specifically by

clonally expanded, most likely tumor-reactive [33], $CD8^+$ T cells that were found more frequently in $HPV16^+IR^+$ tumors. It was also produced by tumor-specific T cells cultured from these tumors. High intratumoral T-cell clonality has previously been positively linked to clinical outcome in melanoma patients treated with ICI.[8] The detection of more clonally expanded T cells in $HPV16^+IR^+$ tumors is suggestive for the accumulation of intratumoral tumor-specific T cells, fitting well with the detection of type 1 $CD4^+$ and $CD8^+$ HPV-specific T cells among the TILs in these IR^+ OPSCC.[2] Our current study suggests that through the production of the chemokines LTB and CCL4, these two types of tumor-specific T cells act as a positive feedback loop for the spatial organization of DC-T cell aggregates, necessary to maintain effective tumor immunity. The discovery of these intratumoral immune microaggregates are of particular importance as potential biomarker in OPSCC, as in this tumor type TLS are not of diagnostic value since they cannot be differentiated from normal lymphoid tissue in which the tumor arises.

In addition to the significant enrichment of CCL4-expressing expanded CD8_0 T cells in $HPV16^+IR^+$ OPSCC tumors, also the clonally expanded clusters CD8_5 and CD4_5 tended to be higher in $HPV16^+IR^+$ OPSCC tumors. Cluster CD8_5 is characterized by the expression of XCL1, known for its capacity to attract cross-presenting DCs into the TME [39], and the clonally expanded $CD4^+$ T-cell cluster is characterized by the expression of *LMNA* (lamin A), which is upregulated early after T cell activation to accelerate the formation of the immunological synapse with APCs [41] and critical for their Th1 differentiation.[42] However, these two clusters also displayed an increased expression of several heat shock protein and stress pathway-related genes. As the expression of such genes may be related to cryopreservation, thawing and dissociation procedures [43], the interpretation of data for these clusters should be done with caution.

The DCs in these microaggregates were defined by their expression of CD11c, CD14 and HLA-DR but not CD68, and co-expressed CD1c, CD32b, CD36, and CD141. The presence of such inflammatory APCs have been linked to acute inflammatory processes [44 45], to the survival of patients with HPV-induced cervical cancer [46] and to immunotherapy responsiveness in HPV-induced premalignant lesions [47 48], while the incapacity to attract these cells constituted a secondary escape mechanism to immunotherapy in a mouse model [49]. Our current findings, showing that these cells are found in higher numbers and organized in immune microaggregates when a tumor-specific T-cell response is present, sustains the notion that these cells are of major

importance in tumor immunity. Currently OPSCC patients are treated by surgery and/or chemoradiation. A therapy associated with high comorbidity and loss in quality of life. The well-organized TIME in HPV16$^+$IR$^+$ OPSCC is likely to promote the response to immunotherapy.[50 51] Notably, the current group of patients treated with ICI after failing standard of care therapy, most likely are those that failed to mount a HPV-specific T-cell response (HPV16$^+$IR$^-$ group) as they will rapidly present with progressive disease.[2] Hence, they will not display the distinct SPS of HPV16$^+$IR$^+$ patients that may make them responsive to ICI. The SPS of HPV16$^+$IR$^+$ OPSCC could be exploited for the identification and selection of this particular patient group, potentially by CD8 and CD11c dual-immunohistochemistry, for neoadjuvant ICI.[37] Alternatively, the mRNA expression profile of IR$^+$ OPSCC could be developed into a suitable selection tool to this purpose.

Imaging mass cytometry showed that the TME in HPV16$^+$IR$^-$ tumors comprises relatively higher number of fibroblasts and blood vessels than HPV16$^+$IR$^+$ OPSCC. Although HPV16$^+$IR$^-$ OPSCC are infiltrated with T cells, albeit it less than in HPV16+IR+ OPSCC, the SPS in these lukewarm tumors was different and comprised spatial interactions between lymphocytes and different subpopulations of immunosuppressive myeloid cells, including CD163$^+$ macrophages, CD204$^+$ macrophages as well as TGFβ$^+$ myeloid cells. This varied per patient, consistent with the lack of coordination of immune cell infiltration in this patient group. Increased expression of the TGFβ superfamily members *INHBA* and *BMP2* [26] were also found in our transcriptomic analyses. The presence of these immune suppressive cells [52-54] and the increased expression of the immune suppressive cytokine *IL-11*, known to suppress the attraction and functionality of tumor-reactive CD4$^+$ T cells [27], potentially explain why tumor-specific T cells were not detected in these tumors. It also provides a rational foundation for combinations of T-cell stimulating agents [6 55 56] with strategies focusing on the identified resistance mechanisms, e.g. co-targeting M2-like macrophages [57], TGFβ [58] and/or angiogenesis [59].

In conclusion, the blueprint of a productive TIME comprises the local production of chemokines that not only attract tumor-reactive CD4$^+$ and CD8$^+$ T cells as well as DCs, but also organize them into small aggregates within the tumor cell beds where most likely the DCs gobble up antigens from dying tumor cells and stimulate the T cells to exercise their effector function and to amplify the immune response.

Supplemental Figures

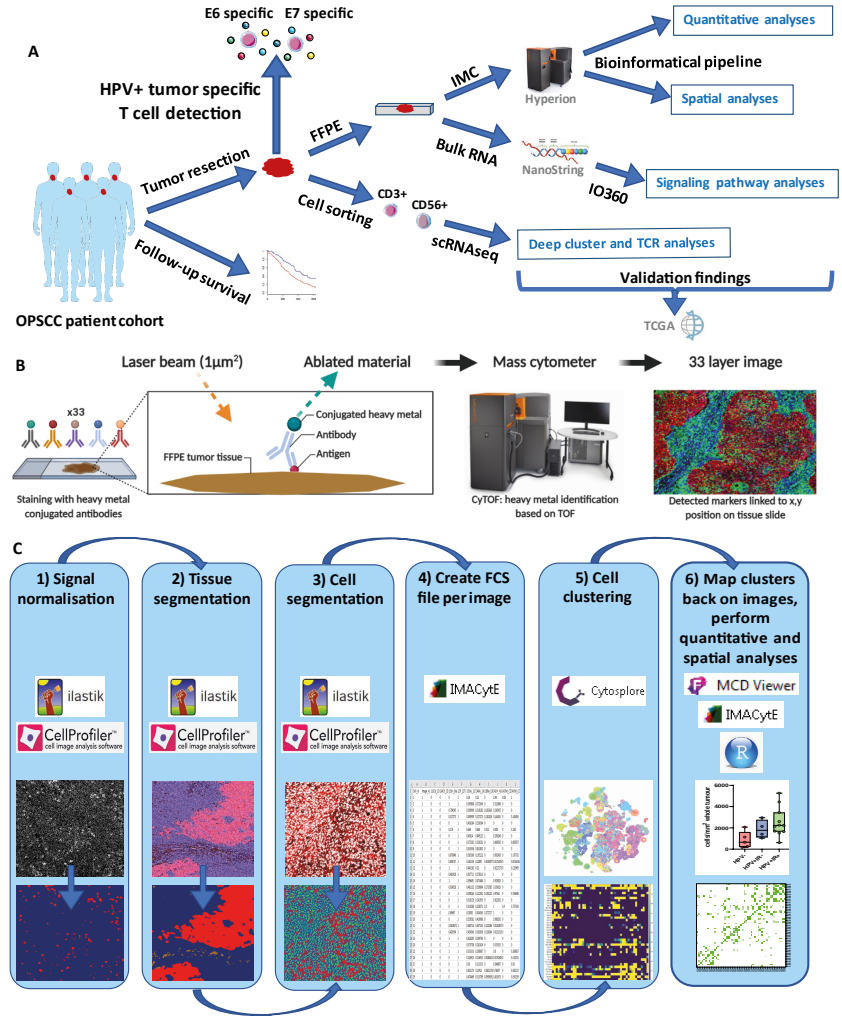

D

	OPSCC total (n=20)	HPV- (n=5)	HPV+IR- (n=4)	HPV+IR+ (n=11)
Immune cells	274,775	45,139	46,204	183,432
Tumor cells	142,868	38,015	37,247	67,606
Stromal cells	46,907	15,149	11,045	20,713
Total cells	464,550	98,303	94,496	271,751

Supplemental Figure 1. Bioinformatical pipeline imaging mass cytometry data analyses.

***A**) Overview of the multi-dimensional study workflow yielding comprehensive high-dimensional information of the immune landscape of Oropharyngeal Squamous Cell Carcinoma (OPSCC). FFPE=formalin-fixed paraffin-embedded; IMC=imaging mass cytometry; scRNAseq=single cell RNA sequencing; TCR=T cell receptor; TCGA=the cancer genome atlas. **B**) Visualization of the imaging mass cytometry staining and image acquisition workflow. Image created with BioRender. **C**) All analytical steps performed to process the imaging mass cytometry data, including the programs used to perform that analytical step, and visualization of the stepwise image processing. **D**) Counts of cells analyzed by imaging mass cytometry in the total OPSCC cohort and per subgroup, of immune cells, tumor cells, stromal cells and the total of all cells analyzed.*

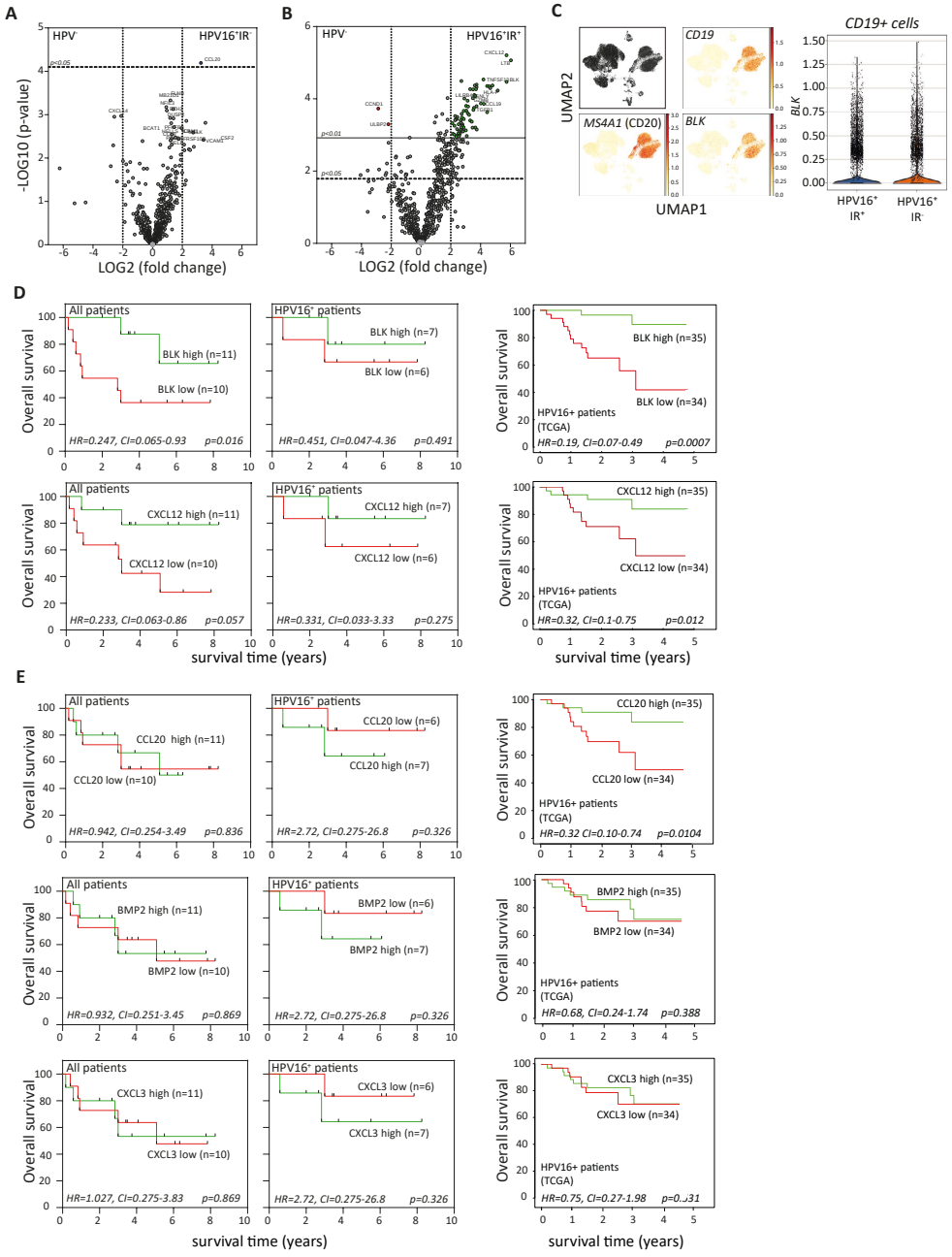

Supplemental Figure 2. Continued

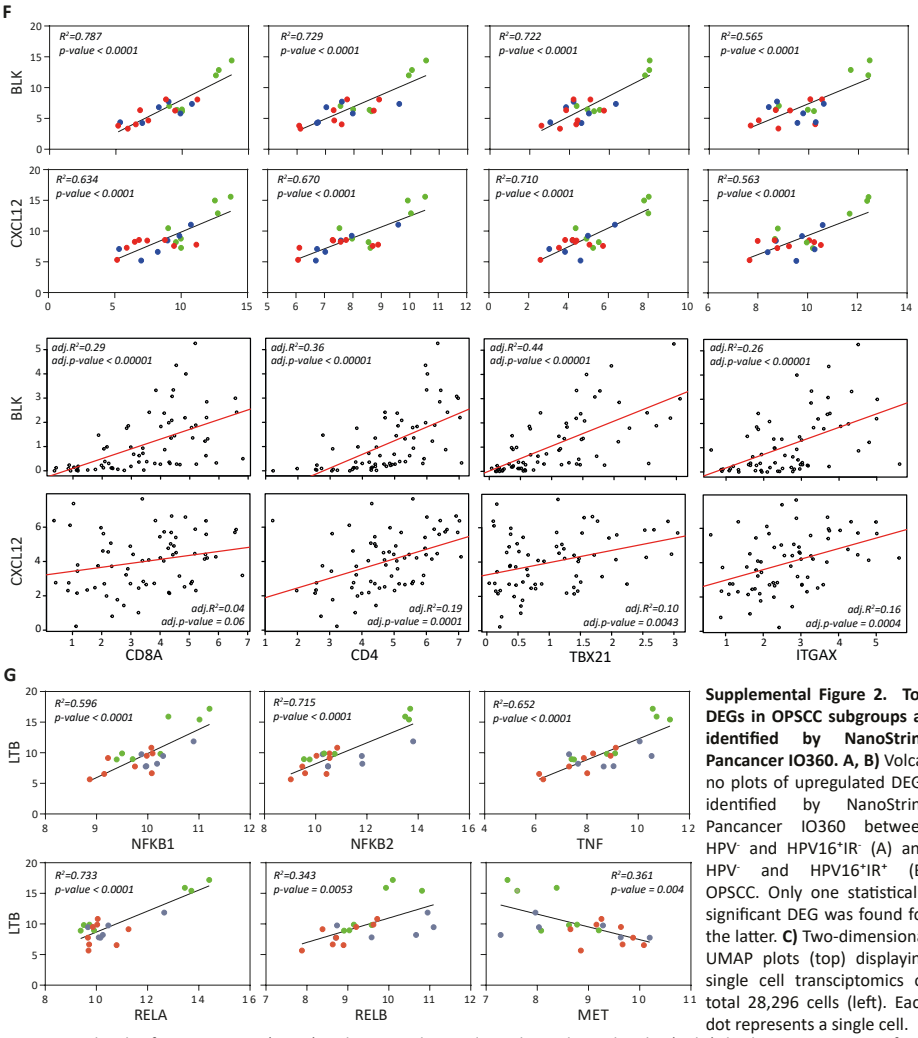

Supplemental Figure 2. Top DEGs in OPSCC subgroups as identified by NanoString Pancancer IO360. A, B) Volcano plots of upregulated DEGs identified by NanoString Pancancer IO360 between HPV$^-$ and HPV16$^+$IR$^-$ (A) and HPV$^-$ and HPV16$^+$IR$^+$ (B) OPSCC. Only one statistically significant DEG was found for the latter. **C)** Two-dimensional UMAP plots (top) displaying single cell transciptomics of total 28,296 cells (left). Each dot represents a single cell. Expression levels of *CD19*, *MS4A1* (CD20) and *BLK* are depicted in color code. Violin plot (right) displaying expression of *BLK* within B cells from HPV16$^+$IR$^+$ (blue; left) and HPV16$^+$IR$^-$ (orange; right) OPSCC. **D)** Kaplan-Meier survival curves based on high/low *BLK* or *CXCL12* expression (classification based on median *BLK* or *CXCL12* expression) upregulated in HPV16$^+$IR$^+$ compared to HPV16$^+$IR$^-$ OPSCC patients for all OPSCC patients analyzed by Nanostring Pancancer IO360 (n=21; left), for the HPV16$^+$ patients within this cohort (n=13; middle), and for a large independent TCGA cohort of HPV16$^+$ OPSCC (n=69; right). **E)** Kaplan-Meier survival curves based on high/low expression of the top 3 DEGs (*CCL20, BMP2 and CXCL3)* upregulated in HPV16$^+$IR$^-$ compared to HPV16$^+$IR$^+$ OPSCC patients for all OPSCC patients analyzed by Nanostring Pancancer IO360 (n=21, left), for the HPV16$^+$ patients within this cohort (n=13; middle), and for a large independent TCGA cohort of HPV16$^+$ OPSCC (n=69; right). **F)** Linear regression analysis of top upregulated DEGs *BLK* and *CXCL12* in HPV16$^+$IR$^+$ compared to HPV16$^+$IR$^-$ OPSCC versus cell type profiles of CD8 (*CD8A*), CD4, Tbet$^+$ T cells (*TBX21*) and DC (*ITGAX*, CD11c). Upper 2 panels display all OPSCC patients analyzed by Nanostring Pancancer IO360 (n=21). Each patient is represented by a colored dot: HPV$^-$ (red), HPV16$^+$IR$^-$ (blue) and HPV16$^+$IR$^+$ (green). The lower 2 panels show the regression analysis of the 69 HPV16$^+$ OPSCC patients of the independent TCGA cohort. **G)** Linear regression analysis of *LTB* versus indicated genes involved in tumor cell migration (metastases) and cell activation.

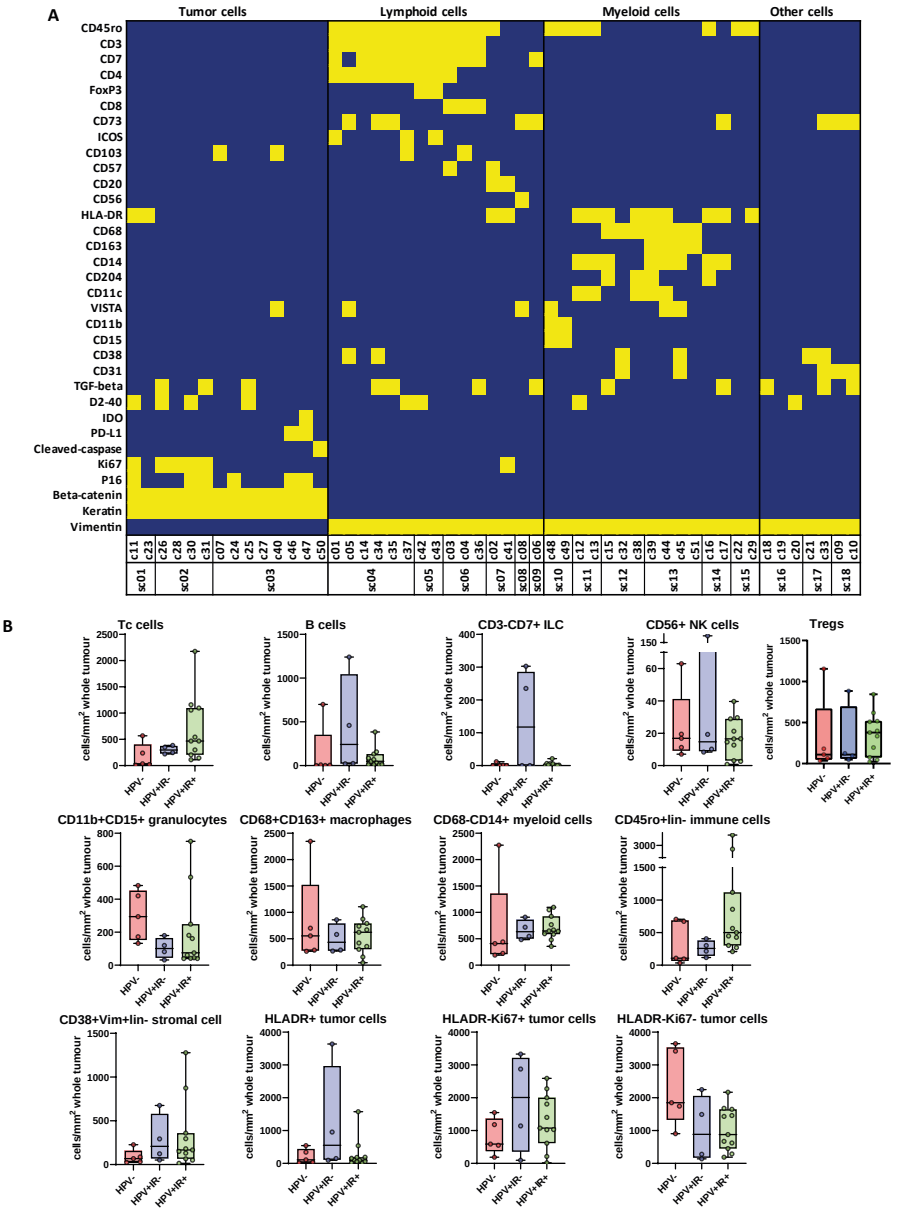

Supplemental Figure 3. Imaging mass cytometry identified (super)clusters in the TME of OPSCC.

Using the unsupervised HSNE-based clustering program Cytosplore, 51 individual cell clusters were identified. ***A****) Heatmap of the verified markers expressed in the identified clusters (c01-c51), and the manual grouping into mutually exclusive superclusters (sc01-sc18).* ***B****) Quantitative comparisons of the remaining 13 of the 18 superclusters present in OPSCC. The three distinct OPSCC subgroups are indicated by different colors: HPV- red (n=5), HPV16+IR- blue (n=4) and HPV16+IR+ green (n=11). Boxplots with bars in box representing the median and interquartile range.*

A

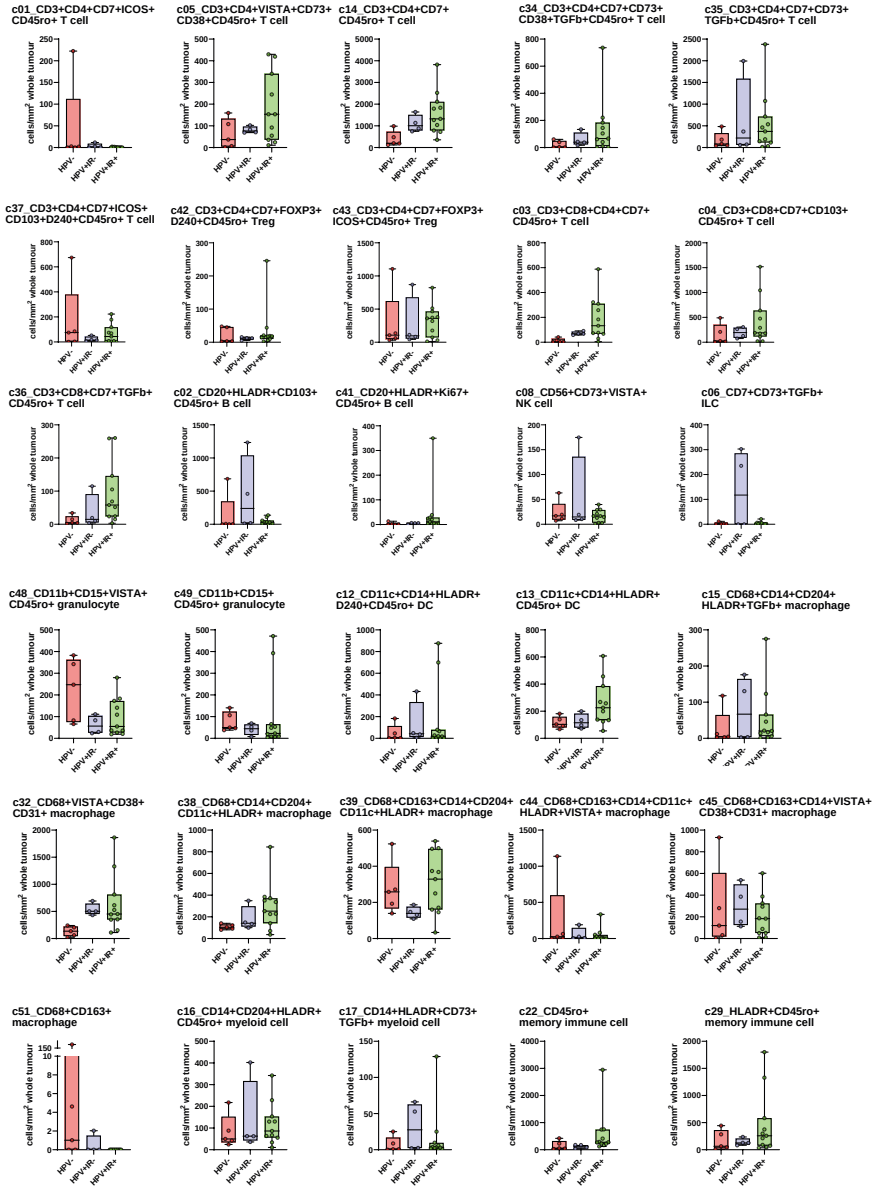

Supplemental Figure 5. Continued

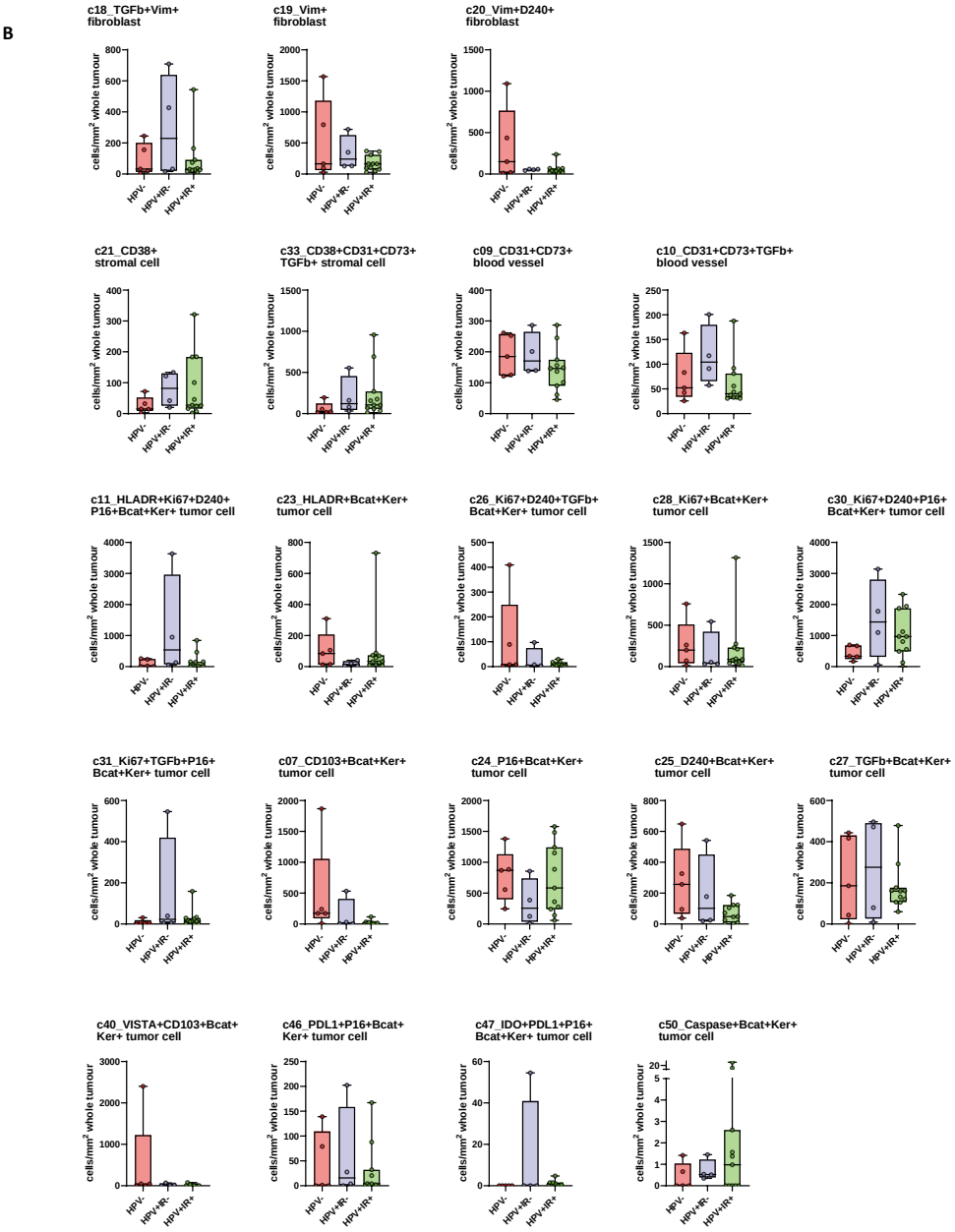

Supplemental Figure 5. Imaging mass cytometry quantitative findings 51 clusters.

*Boxplots showing quantitative comparisons of all 51 identified different cell clusters present in the whole tumor. In **A**) the immune cell clusters and in **B**) the other cell clusters. The three distinct OPSCC subgroups are indicated by different dot colors: HPV- red (n=5), HPV16+IR- blue (n=4) and HPV16+IR+ green (n=11). Boxplots with bars in box representing the median and interquartile range*

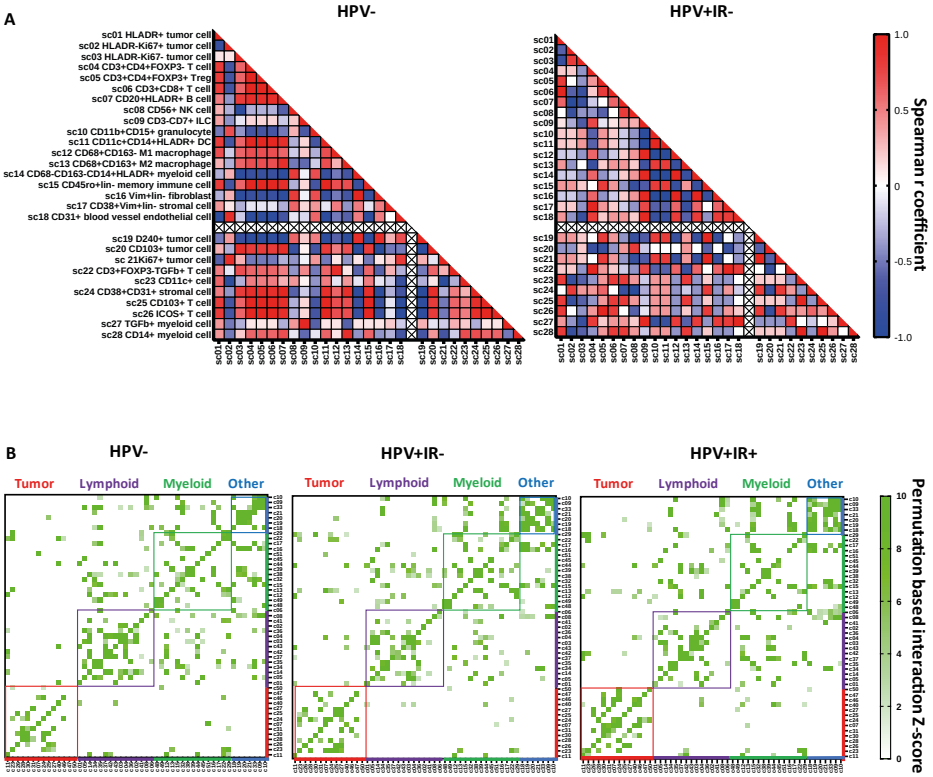

Supplemental Figure 6. Permutation testing of spatial cellular interactions.

***A**) Spearman quantitative correlation heatmaps of the 28 superclusters (18 mutually exclusive, and 10 non-mutually exclusive) in the whole tumor for HPV- (n=5) and HPV16+IR- (n=4) OPSCC. **B**) Heatmap of permutation based Z-scores for spatial interactions between the 51 identified clusters, in HPV- (n=5), HPV16+IR- (n=4) and HPV16+IR+ (n=11) OPSCC. Only interactions with a permutation based Z-score>2 (i.e. outside the 95% normal distribution range) are visualized.*

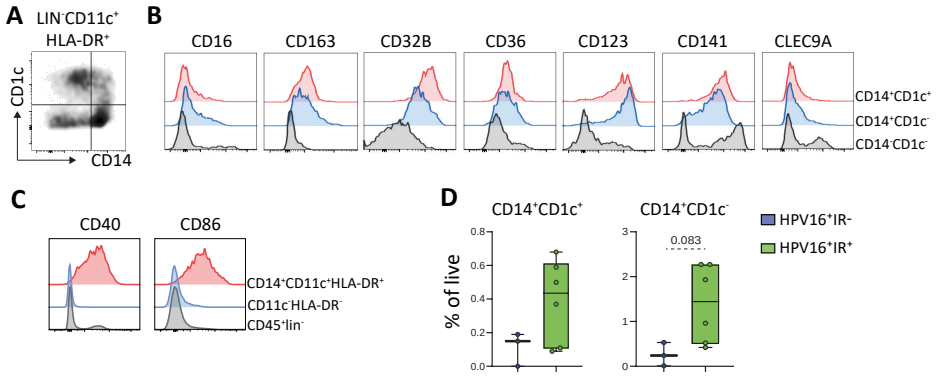

Supplemental Figure 7. Characterization of CD14+CD1c+ DC and CD14+CD1c- monocytes/ macrophages in the TME of HPV16+IR- and HPV16+IR+ OPSCC tumors.

Freshly dissociated OPSCC tumor tissue from 9 HPV16+ OPSCC patients was analyzed by 13-parameter flow cytometry analysis with antibodies directed against CD3/CD19/CD20/CD56, CD11c, HLA-DR, CD14, CD11b, CD163, CD141, CLEC9A, CD1c, CD16, CD123, CD36 and CD32B. ***A***, ***B****) The gating strategy is depicted for a representative OPSCC sample.* ***A****) Dot plot showing expression of CD14 and CD1c within lineage-negative (LIN-), CD11c+ and HLA-DR+ myeloid cells. Singlets were gated on FSC-H/FSC-A properties, atier which dead cells were excluded through gating on yellow amine reactive dye-negative cells. Next, CD3-CD19-CD20-CD56-HLA-DR+CD11c+ myeloid cells were selected, which were subsequently divided based on CD14 and CD1c expression.* ***B****) Histogram plots showing CD16, CD163, CD32B, CD36, CD123, CD141 and CLEC9A expression for CD14-CD1c- (black), CD14+CD1c- (blue) and CD14+CD1c+ cells (red).* ***C****) Histogram plots showing CD40 and CD86 expression for CD45+lin- (black),*
CD11c-HLA-DR- (blue) and CD14+CD11c+HLA-DR+ cells (red). ***D****) Box plots depicting the distribution of the identi- fied CD14+CD1c+ DC (leti) and CD14+CD1c- monocytes/macrophages (right) among HPV16+IR- (blue, n=3) and HPV16+IR+ (green, n=6) OPSCC tumors. Data is represented as percentage of live cells.*

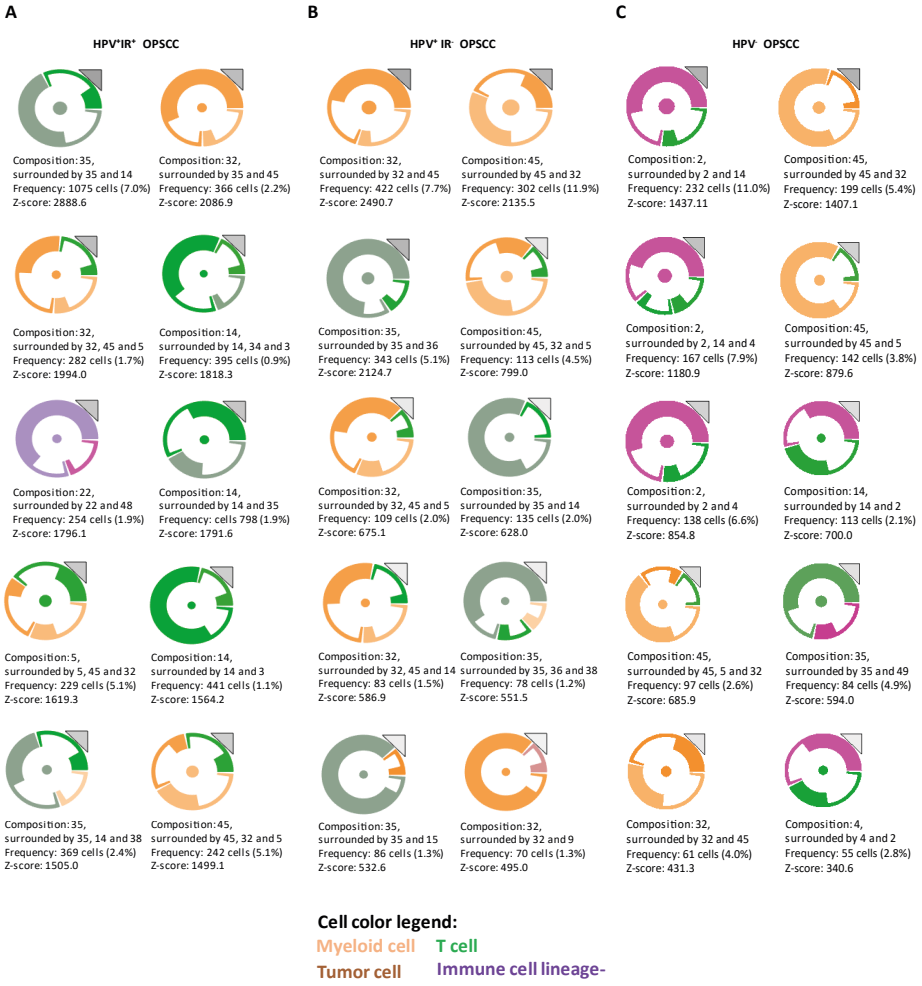

Supplemental Figure 8. Top 10 360° spatial immune compositions per OPSCC subgroup.

*Top 10 360° spatial immune compositions with the highest Z-scores are depicted. In **A**) HPV16+IR+ (n=11), **B**) HPV16+IR- (n=4), and **C**) HPV- (n=5) OPSCC. Clusters, frequency and Z-score are described below each composition. Interaction neighborhood is defined as 5µm (direct spatial cellular interaction). Threshold for the 360° compositions: ≥20 occurrences.*

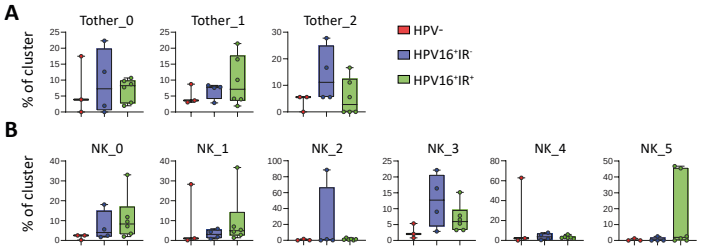

Supplemental Figure 9. Distribution of the identified clusters among HPV-, HPV16+IR- and HPV16+IR+ OPSCC tumors.

*Magnetic-bead sorted CD3+ T cells and CD56+ NK cells from 13 OPSCC samples were analyzed by integrated single-cell transcriptome and TCR repertoire RNA sequencing analysis. Box plots depict the distribution of the Tother (**A**) and NK (**B**) cell clusters among HPV- (red, n=3), HPV16+IR- (blue, n=4) and HPV16+IR+ (green, n=6) OPSCC tumors. Data is represented as percentage of cluster. * p-value<0.05.*

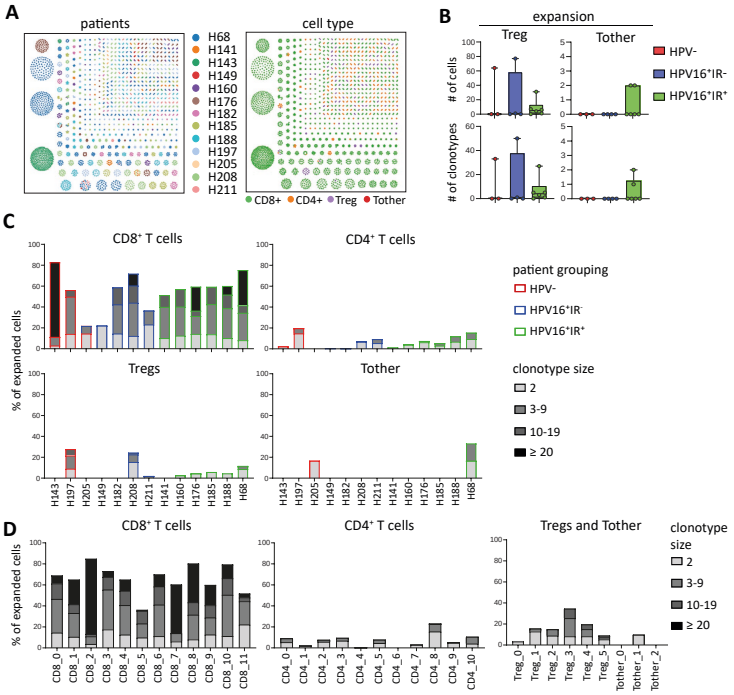

Supplemental Figure 10. Clonotype size among individual OPSCC and T cell clusters. Magnetic-bead sorted CD3+ T cells and CD56+ NK cells from 13 OPSCC samples were analyzed by integrated single-cell transcriptome and TCR repertoire RNA sequencing analysis.

***A**) Graphs depicting the expanded clonotype clusters, colored by patient (left) and cell type (right). **B**) Box plots displaying the number of expanded cells (top) and clonotypes (bottom) within Tregs (left) and Tother (right) cells detected in HPV- (red, n=3), HPV16+IR- (blue, n=4) and HPV16+IR+ (green, n=6) OPSCC patients. **C**, **D**) Graphs depicting the clonotype size of the expanded TCR in CD8+ T cells, CD4+ T cells, Treg and Tother cells per patient (C) and per cluster (D). Data is given as percentage of expanded CD8, CD4, Treg or Tother cells. Colored outline indicates the HPV- and immune response status (HPV- (red, n=3), HPV16+IR- (blue, n=4) and HPV16+IR+ (green, n=6) OPSCC patients).*

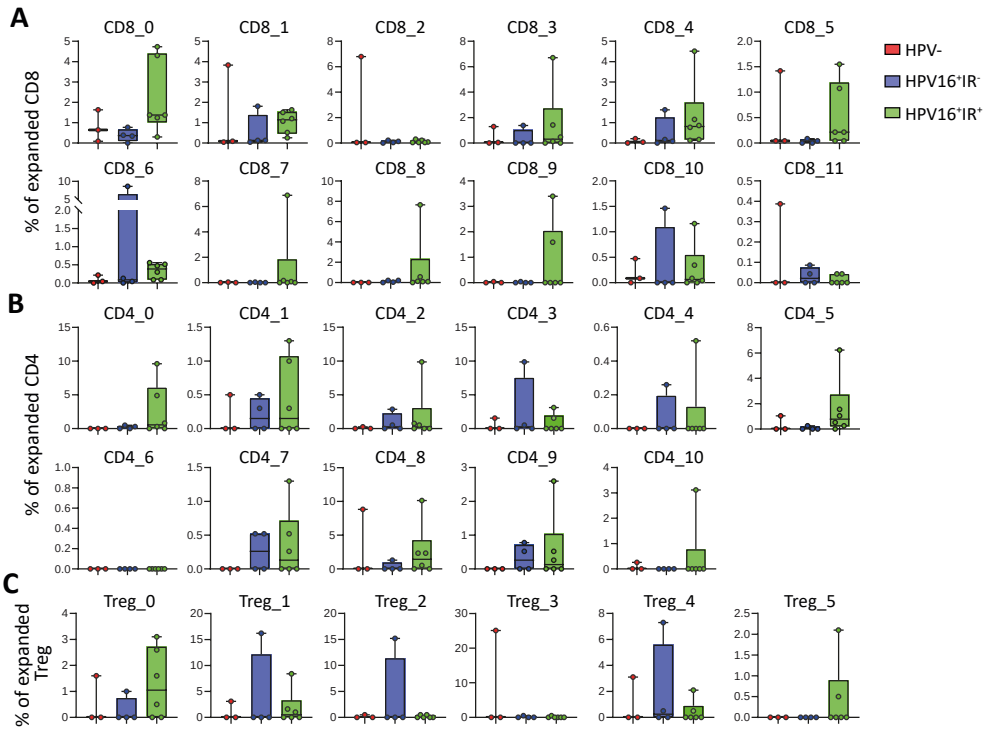

Supplemental Figure 11. T cell expansion among the different T cell clusters.

*Integrated single-cell transcriptome and TCR repertoire RNA sequencing analysis was performed on magnetic- bead sorted CD3+ T cells and CD56+ NK cells from 13 OPSCC samples. A-C) Box plots displaying the percentage of expanded cells within the identified CD8 (**A**), CD4 (**B**) and Treg (**C**) clusters in HPV- (red, n=3), HPV16+IR- (blue, n=4) and HPV16+IR+ (green, n=6) OPSCC patients. Data are represented as percentage of total expanded CD8, CD4 and Treg cells.*

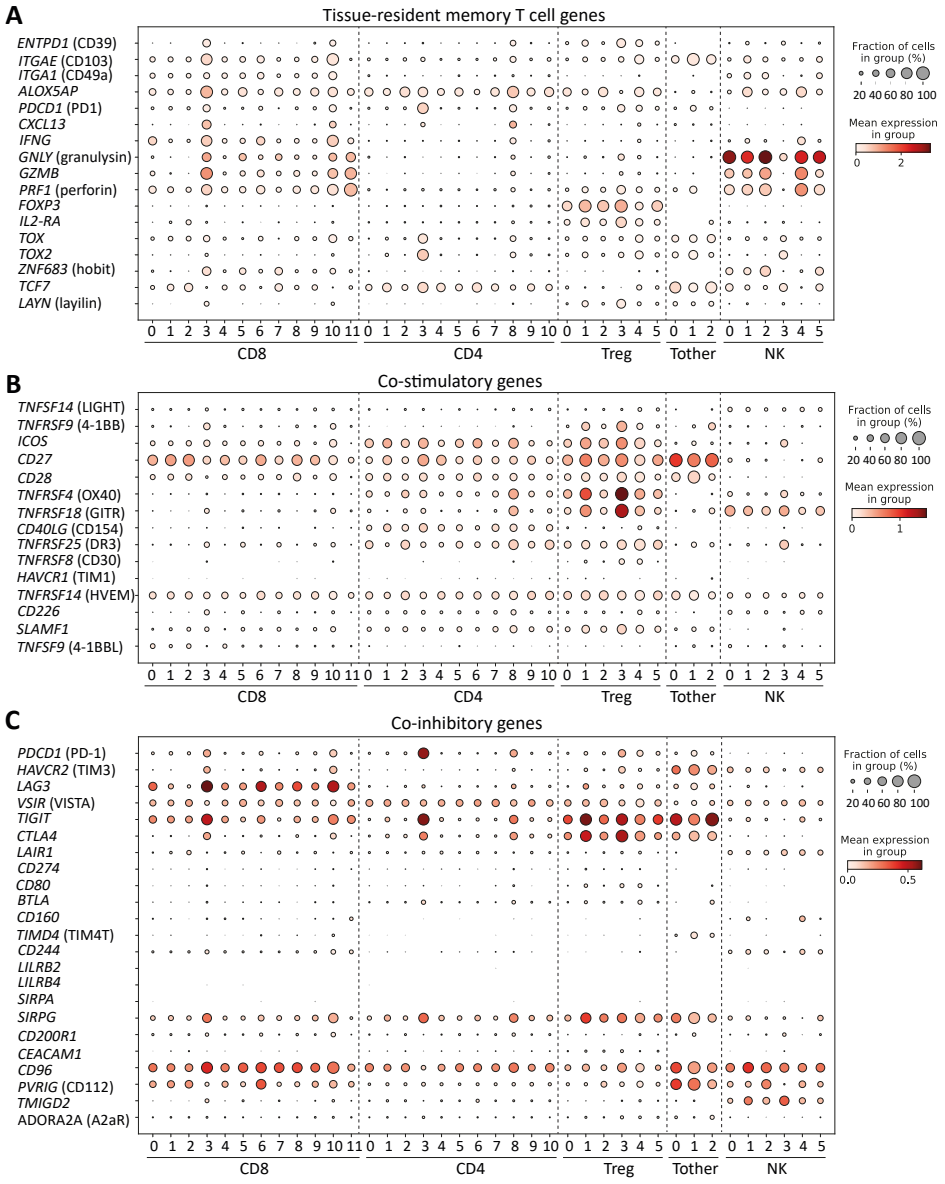

Supplemental Figure 12. Expression of tissue-resident memory T cell, co-stimulatory and co-inhibitory markers within the intratumoral CD8, CD4, Treg, Tother and NK cell cluster in OPSCC.

*Single-cell transcriptome RNA sequencing analysis was performed on magnetic-bead sorted CD3+ T cells and CD56⁺ NK cells from 13 OPSCC samples. Dot plots depict the expression levels of **A**) tissue-resident memory T cell, **B**) co-stimulatory and **C**) co-inhibitory genes (Y-axis) for all identified CD8, CD4, Treg, Tother and NK clusters (X-axis, from left to right). The size of the dots represent the percentage of cells expressing the genes, and the color scale*
indicates the mean expression of the genes.

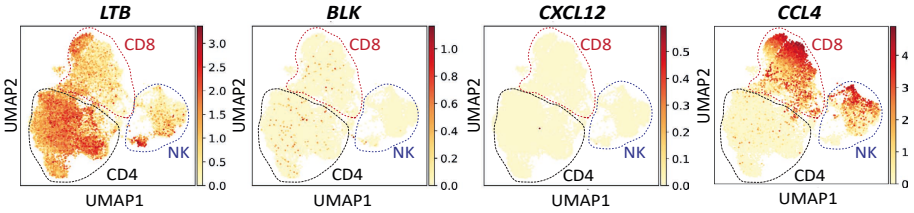

Supplemental Figure 13. Expression of LTB, BLK, CXCL12, CCL4, XCL1 and LMNA within T cells and NK cells.

Two-dimensional UMAP plots displaying single cell transciptomics of 14,242 T cells and 2,820 NK cells from 13 OPSCC patients. Each dot represents a single cell. Expression levels of LTB, BLK, CXCL12 and CCL4 are depicted in color code. Dotted borders denote where CD4, CD8 and NK cell clusters are located.

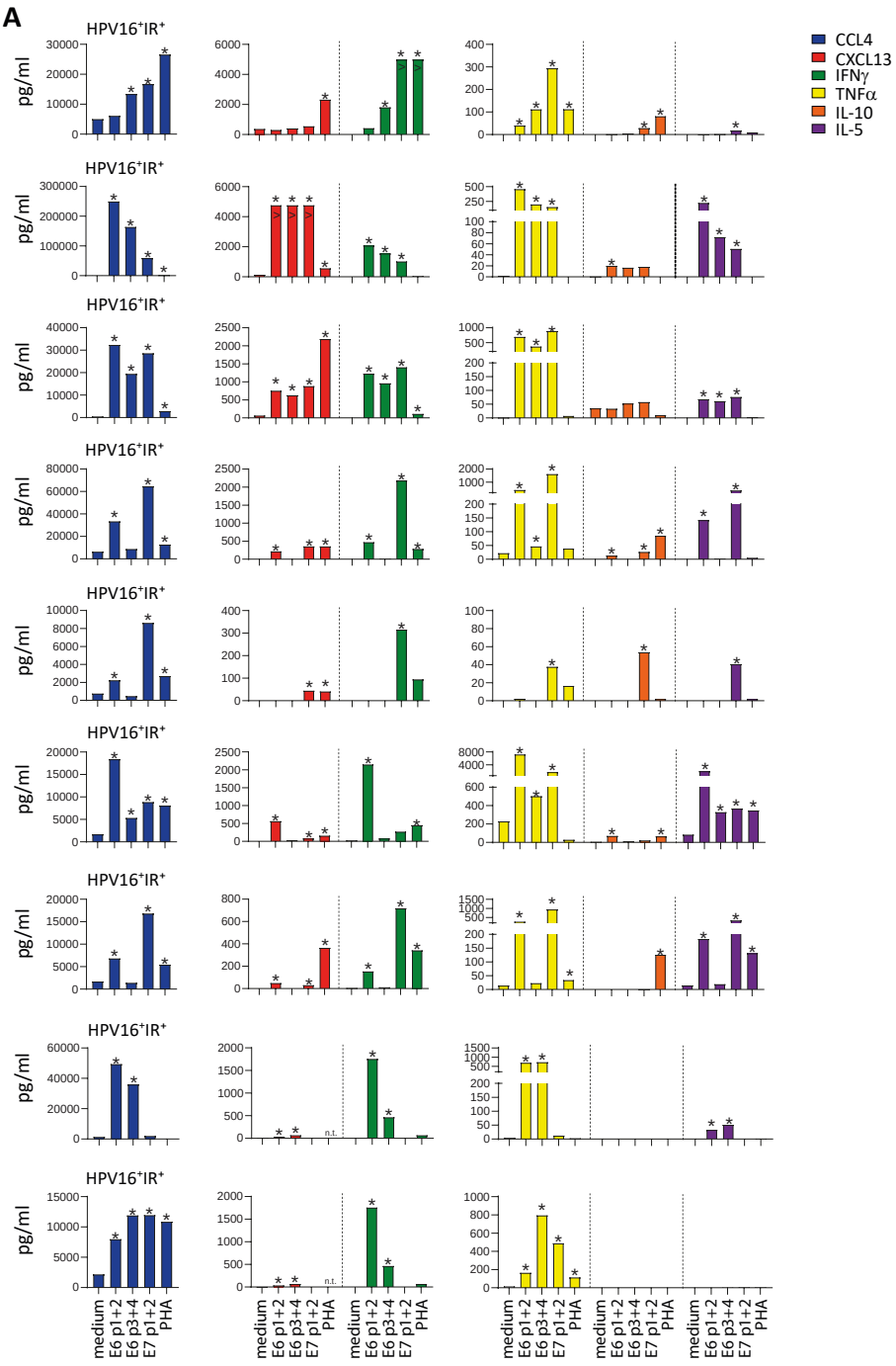

Supplemental Figure 14. Continued

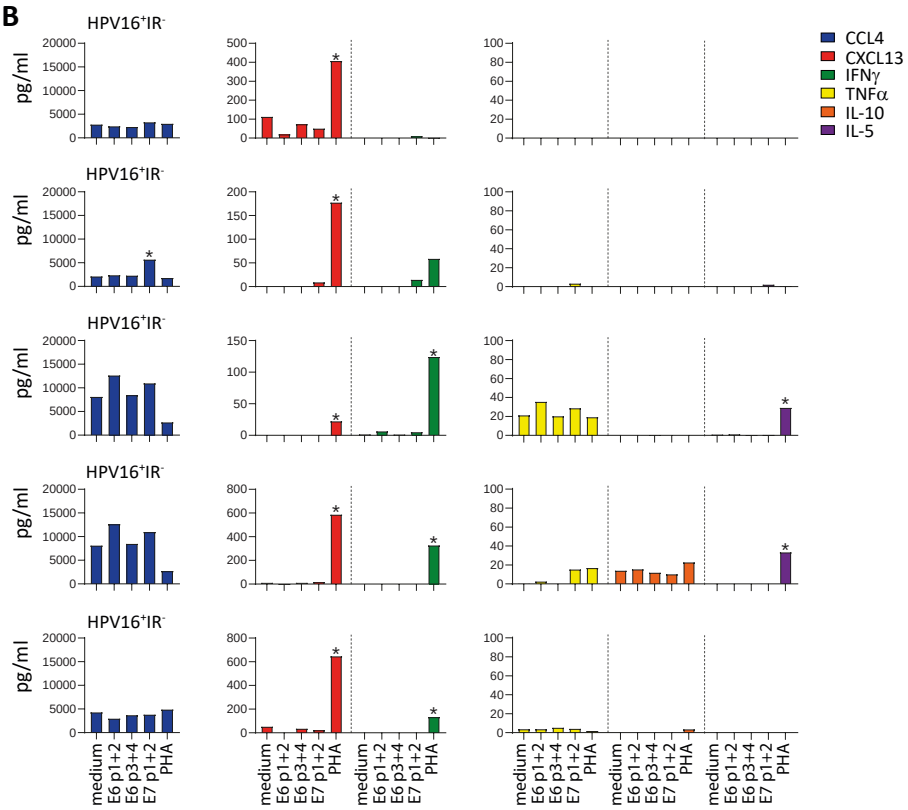

Supplemental Figure 14. HPV reactivity of cultured OPSCC TIL.

*Graphs displaying CCL4 (blue), CXCL13 (red), IFNγ (green), TNFα (yellow), IL-10 (orange) and IL-5 (purple) production of cultured OPSCC TIL in response to medium, HPV16 E6 peptide (pool 1+2 and 3+4), HPV16 E7 peptide (pool 1+2)-loaded autologous monocytes for HPV16⁺IR⁺ (n=9; **A**) and HPV16⁺IR- (n=5; **B**) OPSCC. Cytokine production in response to PHA served as positive control. Positive cytokine production, which is defined as at least twice above that of the cells stimulated with medium-loaded monocytes, is indicated by the asterisk. CCL4 and CXCL13 were determined by a multiplex cytokine assay and IFNγ, TNFα, IL-10 and IL-5 by cytometric bead array.*

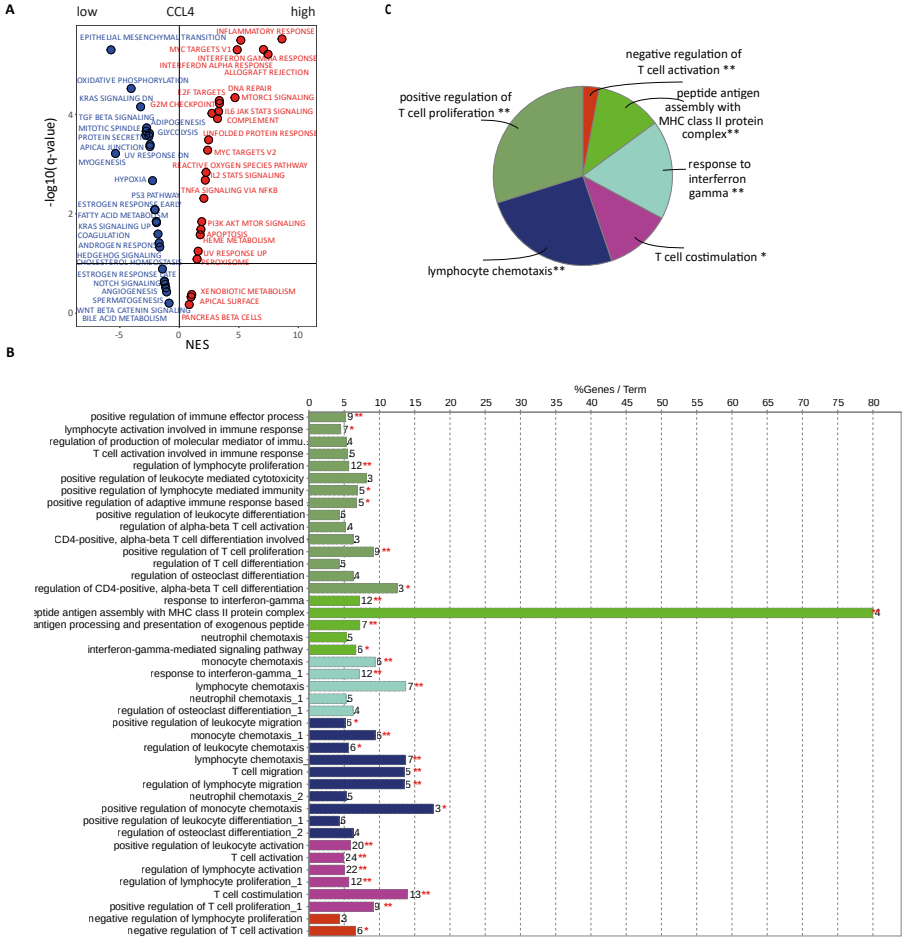

Supplemental Figure 15. CCL4 expression is associated with a productive tumor immune microenvironment.

***A**) High expression of CCL4 is positively associated with the hallmark gene sets of tumor rejection and negatively associated with the hallmarks of tumor promotion. The log2 fold change level of each gene between a high and low group was used as input for the GSEA-preranked. The GSEA was performed using the Molecular Signatures Database (MSigDB). The 50 hallmark gene sets were illustrated by their normalized enrichment score (NES). Red and blue dots show the enrichment and depletion of hallmark gene sets, respectively. **B**) ClueGO analysis of highly significant associated genes with high expression of CCL4 in the tumor microenvironment (R>0.7 and R>0.4, respectively, adj-value <0.05). The bars represent the percentage of highly significantly correlated genes associated with the GO terms (%Genes/term). The number of expressed genes per term is shown as bar label. P-value is indicated by asterisks. **C**) Overview chart with functional groups including specific terms for highly significantly associated genes with high expression of CCL4. * mid-P values of two-sided (enrichment/depletion) tests based on the hyper geometric distribution (Rivals, 2007, PMID. 17182697).*

Supplemental Tables

Supplemental Table 1. OPSCC patient characteristics.

Patient ID *	Sex	Age **	Tumor location	pTNM stage	HPV16 status	IR status ***	Received treatment	Analysis techniques
H62	M	61	Tongue base	4a-2c-0	+	-	RT	NanoString
H68	F	64	Tonsil	3-2b-0	+	+	RT	Hyperion, scRNAseq, NanoString, Luminex
H71	F	62	Tongue base	2-2c-0	+	+	RT	Hyperion, NanoString
H72	M	58	Tongue base	2-0-0	-	-	RT	Hyperion, NanoString
H74	F	65	Tonsil	4a-0-0	-	-	none	Hyperion, NanoString
H77	M	48	Tonsillar fossa	1-2a-0	+	+	S+RT	Hyperion, NanoString
H78	M	54	Tonsillar fossa	2-0-0	-	-	RT	NanoString
H93	M	57	Tongue base	1-2b-0	+	+	S+RT	Hyperion, NanoString
H95	M	59	Tongue base	2-1-0	+	+	RT	NanoString
H125	M	64	Posterior wall	3-0-0	-	-	CT+RT	NanoString
H136	V	47	Tonsil	2-2b-0	+	+	CT+RT	Hyperion, NanoString, Luminex
H138	M	74	Tongue base	2-0-0	+	+	RT	Hyperion, Luminex
H141	M	67	Tongue base	2-2b-0	+	+	CT+RT	Hyperion, scRNAseq, NanoString
H143	V	74	Tonsil	1-2a-0	-	-	RT	Hyperion, scRNAseq, NanoString
H148	V	64	Tonsil	2-2b-0	+	+	S+RT	Luminex
H149	V	47	Tonsil	2-2a-0	+	-	S+RT	Hyperion, scRNAseq, NanoString, Luminex
H150	M	59	Tonsil	2-2a-0	+	-	S+RT	Luminex
H159	V	67	Tonsil	4a-2c-0	+	+	CT+RT	Luminex
H160	M	69	Tongue base	2-2b-0	+	+	CT+RT	Hyperion, scRNAseq, NanoString, Luminex
H161	V	65	Tongue base	2-2b-0	+	+	S+RT	Luminex

Supplemental Table 1 *Continued*

Patient ID *	Sex	Age **	Tumor location	pTNM stage	HPV16 status	IR status ***	Received treatment	Analysis techniques
H176	M	52	Tongue base	3-0-0	+	+	CT+RT	Hyperion, scRNAseq, NanoString
H180	M	59	Tonsil	2-2a-0	+	+	RT	Luminex
H182	M	66	Tongue base	4-3-0	+	-	CT	Hyperion, scRNAseq, NanoString
H185	M	58	Tongue base	2-0-0	+	+	RT	Hyperion, scRNAseq, NanoString
H187	V	67	Pallatum mole	2-0-0	-	-	RT	NanoString
H188	V	56	Tonsil	3-0-0	+	+	CT+RT	Hyperion, scRNAseq, NanoString, Luminex
H191	M	39	Tonsil	2-2b-0	+	-	RT	Luminex
H197	V	63	Tonsil	4b-0-0	-	-	CT+RT+CX	Hyperion, scRNAseq, NanoString
H205	M	56	Tonsil	4a-2b-1	-	-	RT	Hyperion, scRNAseq, NanoString
H208	M	60	Tongue base	4-2a-0	+	-	CT+RT	Hyperion, scRNAseq, NanoString, Luminex
H211	M	62	Tongue base	3-2b-0	+	-	CT+RT	Hyperion, scRNAseq, NanoString, Luminex

** 'H' indicates OPSCC patients included in the P07-112 head and neck cancer study*
*** Age at diagnosis and sampling of tumor tissue pre-therapy*
**** Immune response (IR) status was determined by analyzing cultured tumor infiltrating lymphocytes for the presence of HPV16-specific T cells using a [3H]-thymidine-based proliferation assay and antigen-specific cytokine production assay*
CT: chemotherapy; CX: cetuximab; F: female; M: male; pTNM: pathological Tumor, lymph Nodes, Metastasis; RT: radiotherapy; S: surgical resection

Supplemental Table 2. Definition of NanoString nSolver cell types.

Cell type	Gene
CD45	*PTPRC*
T cells	*CD3D*
	CD3E
	CD3G
	CD6
	SH2D1A
	TRAT1
B cells	*BLK*
	CD19
	FCRL2
	MS4A1
	PNOC
	SPIB
	TCL1A
	TNFRSF17
DC	*CCL13*
	CD209
	HSD11B1
CD8	*CD8A*
	CD8B
Th1	*TBX21*
Treg	*FOXP3*
Exhausted CD8	*CD244*
	EOMES
	LAG3
	PTGER4
Cytotoxic cell	*CTSW*
	GNLY
	GZMA
	GZMB
	GZMH
	KLRB1
	KLRD1
	KLRK1
	NKG7
	PRF1
Macrophage	*CD163*
	CD68
	CD84
	MS4A4A
Neutrophils	*CEACAM3*
	CSF3R
	FCAR
	FPR1
	S100A12
	SIGLEC5
NK cells	*NCR1*
NK CD56dim	*IL21R*
	KIR2DL3
	KIR3DL1
	KIR3DL2
Mast cells	*CPA3*
	HDC
	MS4A2

Cell types as automatically defined by the expression of the indicated genes by NanoString nSolver software

Supplemental Table 3. Imaging mass cytometry 33-marker panel.

Marker	Antibody clone	Conjugated heavy metal	Antibody dilution	Incubation conditions
HLA-DR	TAL1B5	^{141}Pr	1:100	5 hours at room temperature
CD11b	D6X1N	^{144}Nd	1:100	5 hours at room temperature
CD4	EPR6855	^{145}Nd	1:50	5 hours at room temperature
CD8	D8A8Y	^{146}Nd	1:50	5 hours at room temperature
CD73	D7F9A	^{148}Nd	1:100	5 hours at room temperature
TGFβ	TB21	^{149}Sm	1:100	5 hours at room temperature
PD-L1	E1L3N(R)	^{156}Gd	1:100	5 hours at room temperature
FoxP3	D608R	^{159}Tb	1:100	5 hours at room temperature
IDO	D5J4E(TM)	^{162}Dy	1:50	5 hours at room temperature
CD204	J5HTR3	^{164}Dy	1:100	5 hours at room temperature
CD45ro	UCHL1	^{165}Ho	1:50	5 hours at room temperature
CD38	EPR4106	^{169}Tm	1:50	5 hours at room temperature
CD163	EPR14643-36	^{173}Yb	1:100	5 hours at room temperature
CD7	EPR4242	^{174}Yb	1:50	5 hours at room temperature
P16	D3W8G	^{175}Lu	1:100	5 hours at room temperature
Vimentin	D21H3	^{194}Pt	1:100	5 hours at room temperature
β-catenin	D10A8	^{115}In	1:100	overnight at 4 degrees Celsius
CD20	H1	^{142}Nd	1:100	overnight at 4 degrees Celsius
CD68	D4B9C	^{143}Nd	1:100	overnight at 4 degrees Celsius
CD31	89C2	^{147}Sm	1:100	overnight at 4 degrees Celsius
CD57	HNK-1/Leu-7	^{151}Eu	1:100	overnight at 4 degrees Celsius
Ki67	8D5	^{152}Sm	1:100	overnight at 4 degrees Celsius
CD3	D7AGE(TM)	^{153}Eu	1:50	overnight at 4 degrees Celsius
VISTA	D1L2G(TM)	^{158}Gd	1:50	overnight at 4 degrees Celsius
ICOS	D1K2T(TM)	^{161}Dy	1:50	overnight at 4 degrees Celsius
CD14	D7A2T	^{163}Dy	1:100	overnight at 4 degrees Celsius
D2-40	D2-40	^{166}Er	1:100	overnight at 4 degrees Celsius
CD56	EPR2566	^{167}Er	1:100	overnight at 4 degrees Celsius
CD103	EPR4166(2)	^{168}Er	1:100	overnight at 4 degrees Celsius
CD15	BRA-4F1	^{171}Yb	1:100	overnight at 4 degrees Celsius
Cleaved-caspase	ASP175	^{172}Yb	1:100	overnight at 4 degrees Celsius
CD11c	EP1347Y	^{176}Yb	1:100	overnight at 4 degrees Celsius
Keratin	C11 and AE1/AE3	^{198}Pt	1:50	overnight at 4 degrees Celsius

Supplemental Table 4A. Differentially expressed genes (DEGs) between HPV16+IR+ and HPV16+IR- OPSCC patients.

DEG	Log2 fold change	SD	P-value	Method	Corrected P-value
CCL20	-3.67	0.647	2.20E-05	Lm.nb	0.0124
BMP2	-2.68	0.512	5.60E-05	Lm.nb	0.0124
BLK	5.85	1.13	6.35E-05	Lm.nb	0.0124
HLA-DRB1	3.55	0.705	8.73E-05	Lm.nb	0.0124
CXCL3	-3.25	0.652	9.56E-05	Lm.nb	0.0124
LTB	5.22	1.06	0.00011	Lm.nb	0.0124
PFKFB3	-1.69	0.347	0.000123	Lm.nb	0.0124
CXCL12	4.59	0.98	0.000186	Lm.nb	0.0164
CCL19	4.1	0.943	0.000386	Lm.nb	0.028
CSF2	-4.26	0.984	4.00E-04	Lm.nb	0.028
TNFSF13	4.08	0.962	0.000489	Lm.nb	0.028
NLRC5	1.84	0.439	0.000539	Lm.nb	0.028
HLA-DQA2	-6.12	1.45	0.000586	Wald	0.028
HSD11B1	3.21	0.771	0.000639	Wald	0.028
TNFRSF18	3.71	0.9	0.00064	Lm.nb	0.028
PIK3CD	3.03	0.745	0.000721	Lm.nb	0.028
HLA-A	2.87	0.706	0.000737	Lm.nb	0.028
TREM1	-2.56	0.633	0.000762	Lm.nb	0.028
INHBA	-3.93	0.98	0.000819	Lm.nb	0.028
IL1B	-3.16	0.791	0.000834	Lm.nb	0.028
LILRB4	3	0.751	0.000837	Lm.nb	0.028
HRAS	3.66	0.921	0.000891	Lm.nb	0.028
KLRD1	3.38	0.845	0.000913	Wald	0.028
CXCL8	-3.65	0.928	0.000968	Lm.nb	0.0285
IL11	-3.43	0.885	0.00112	Lm.nb	0.0308
IKBKB	2.79	0.724	0.00115	Lm.nb	0.0308
HLA-F	3.62	0.946	0.00123	Lm.nb	0.0308
CD79A	3.74	0.985	0.00132	Lm.nb	0.0308
TNFSF9	3.57	0.931	0.00132	Wald	0.0308
APOL6	2.87	0.755	0.00132	Lm.nb	0.0308
CD58	2.59	0.684	0.00135	Lm.nb	0.0308
PNOC	2.84	0.75	0.00148	Wald	0.0325
IRF5	1.55	0.417	0.00156	Lm.nb	0.0325
NEIL1	2.11	0.569	0.00159	Lm.nb	0.0325
IRF4	2.97	0.801	0.00161	Lm.nb	0.0325
IL6R	2.16	0.586	0.00167	Lm.nb	0.0326
LYZ	1.79	0.487	0.00171	Lm.nb	0.0326
CD6	2.59	0.709	0.0018	Lm.nb	0.0329
PGPEP1	2.61	0.715	0.00182	Lm.nb	0.0329
GZMM	2.41	0.656	0.0019	Wald	0.0336
PSMB10	2.03	0.577	0.00246	Lm.nb	0.0424
CTSW	2.79	0.798	0.00258	Lm.nb	0.0434
TGFB1	2.9	0.845	0.00295	Lm.nb	0.0474

Supplemental Table 4B. Differentially expressed genes (DEGs) between HPV16+IR- and HPV- OPSCC patients.

DEG	Log2 fold change	SD	P-value	Method	Corrected P-value
CCL20	3.25	0.628	6.43E-05	lm.nb	0.0454

Supplemental Table 4C. Differentially expressed genes (DEGs) between HPV16+IR+ and HPV- OPSCC patients.

DEG	Log2 fold change	SD	P-value	Method	Corrected P-value
CXCL12	5.74	0.912	6.21E-06	lm.nb	0.00259
LTB	6.04	0.986	8.60E-06	lm.nb	0.00259
KLRD1	4.19	0.743	2.92E-05	Wald	0.00259
BBC3	2.71	0.493	3.22E-05	lm.nb	0.00259
BLK	5.75	1.05	3.40E-05	lm.nb	0.00259
PIK3CD	3.73	0.693	4.06E-05	lm.nb	0.00259
TNFSF13	4.8	0.895	4.28E-05	lm.nb	0.00259
IKBKB	3.61	0.673	4.29E-05	lm.nb	0.00259
UBA7	4.44	0.831	4.42E-05	lm.nb	0.00259
HRAS	4.57	0.856	4.49E-05	lm.nb	0.00259
APOL6	3.73	0.702	4.77E-05	lm.nb	0.00259
HLA-F	4.65	0.88	5.06E-05	lm.nb	0.00259
C5	3.3	0.628	5.40E-05	lm.nb	0.00259
DNMT1	3.69	0.703	5.43E-05	lm.nb	0.00259
DDB2	3.49	0.666	5.50E-05	lm.nb	0.00259
ICAM5	5.15	0.988	5.89E-05	lm.nb	0.0026
GNLY	3.58	0.704	7.82E-05	lm.nb	0.00325
GZMB	3.65	0.712	8.35E-05	Wald	0.00327
POLD1	1.78	0.357	9.52E-05	lm.nb	0.00329
LILRB4	3.48	0.698	9.58E-05	lm.nb	0.00329
VHL	2.91	0.586	9.77E-05	lm.nb	0.00329
CD58	3.13	0.637	0.000113	lm.nb	0.00362
GLS	4.02	0.831	0.000134	lm.nb	0.00406
CCL19	4.22	0.877	0.000138	lm.nb	0.00406
DLL4	3.03	0.636	0.000157	lm.nb	0.00426
TGFB1	3.73	0.786	0.00016	lm.nb	0.00426
PGPEP1	3.16	0.666	0.000163	lm.nb	0.00426
MSH6	3.56	0.757	0.000177	lm.nb	0.00446
CCND1	-2.87	0.612	0.000186	lm.nb	0.00453
PIK3R2	3.52	0.758	0.000203	lm.nb	0.00477
CTLA4	3.04	0.659	0.000212	lm.nb	0.00477
CSF1	2.87	0.623	0.000216	lm.nb	0.00477
NLRP3	4.44	0.97	0.000235	lm.nb	0.00503
CD7	3.14	0.691	0.000252	lm.nb	0.00516
CD80	2.73	0.604	0.000261	lm.nb	0.00516
IRF7	1.43	0.316	0.000263	lm.nb	0.00516
HSD11B1	3.23	0.707	0.000277	Wald	0.00529
FANCA	2.29	0.513	0.000301	lm.nb	0.00559
EZH2	1.02	0.228	0.000309	lm.nb	0.0056

DEG	Log2 fold change	SD	P-value	Method	Corrected P-value
IRF1	2.44	0.549	0.000318	lm.nb	0.0056
CSF2RB	2.75	0.622	0.00033	lm.nb	0.00568
JAK2	2.41	0.55	0.000361	lm.nb	0.00585
HLA-DRB1	2.87	0.656	0.000364	lm.nb	0.00585
NLRC5	1.78	0.408	0.000377	lm.nb	0.00585
NOTCH1	2.32	0.531	0.000377	lm.nb	0.00585
TNFRSF25	2.29	0.526	0.000389	lm.nb	0.00585
CHUK	2.66	0.611	0.000393	lm.nb	0.00585
AXL	3.3	0.761	0.000397	lm.nb	0.00585
JAG2	3.41	0.782	0.000427	Wald	0.00615
MB21D1	0.921	0.215	0.000455	lm.nb	0.00632
CCL18	2.68	0.626	0.000456	lm.nb	0.00632
PPARGC1B	2.1	0.494	0.000472	lm.nb	0.00641
ULBP2	-2.19	0.518	0.000505	lm.nb	0.00654
TMEM140	2.53	0.599	0.000507	lm.nb	0.00654
CYBB	2.78	0.657	0.000509	lm.nb	0.00654
PSMB10	2.25	0.537	0.000555	lm.nb	0.00689
LGALS9	2.78	0.664	0.000557	lm.nb	0.00689
NCR1	2.86	0.682	0.000616	Wald	0.00729
CD68	2.7	0.653	0.000617	lm.nb	0.00729
TNFSF9	3.65	0.873	0.000622	Wald	0.00729
TNFRSF18	3.46	0.837	0.000629	lm.nb	0.00729
RAD51C	2.42	0.591	0.000687	lm.nb	0.00782
CD79A	3.74	0.916	0.000707	lm.nb	0.00792
SIGLEC1	2.65	0.651	0.00073	lm.nb	0.00805
CTSW	3.01	0.743	0.000747	lm.nb	0.00811
PVRIG	2.82	0.699	0.000776	lm.nb	0.0082
MLH1	1.72	0.427	0.000791	lm.nb	0.0082
TIE1	2.82	0.7	0.000798	lm.nb	0.0082
BRD3	2.56	0.638	0.000801	lm.nb	0.0082
MTOR	1.32	0.333	0.000892	lm.nb	0.00885
CD6	2.62	0.659	0.000898	lm.nb	0.00885
TYMS	2.51	0.632	0.000902	lm.nb	0.00885
MELK	1.17	0.295	0.000918	lm.nb	0.00887
IL6R	2.15	0.545	0.00093	lm.nb	0.00887
NFAM1	2.24	0.564	0.000978	Wald	0.00911
TAP2	1.62	0.413	0.00098	lm.nb	0.00911
CD74	2.57	0.656	0.00102	lm.nb	0.00936
JAK3	2.42	0.622	0.00106	lm.nb	0.00958
ZAP70	3.07	0.789	0.00107	lm.nb	0.00958
RELA	2.53	0.652	0.0011	lm.nb	0.0097
NFKB2	2.37	0.612	0.00112	lm.nb	0.00973
BAX	1.24	0.322	0.00115	lm.nb	0.00991
CDK2	1.5	0.393	0.00127	lm.nb	0.0107
TNFRSF1B	2.14	0.563	0.00132	lm.nb	0.0108
IRF3	1.18	0.312	0.00136	lm.nb	0.0108
ITGAL	2.82	0.745	0.00136	lm.nb	0.0108
STAT2	1.13	0.298	0.00137	lm.nb	0.0108
HLA-C	2.67	0.708	0.00138	lm.nb	0.0108

Supplemental Table 4C *Continued*

DEG	Log2 fold change	SD	P-value	Method	Corrected P-value
HLA-DMA	2.4	0.637	0.00139	lm.nb	0.0108
HELLS	1.45	0.385	0.0014	lm.nb	0.0108
SBNO2	1.25	0.331	0.0014	lm.nb	0.0108
IRF4	2.78	0.745	0.00153	lm.nb	0.0113
FUT4	2.68	0.72	0.00153	lm.nb	0.0113
CD3D	2.84	0.762	0.00156	lm.nb	0.0113
DUSP5	1.52	0.409	0.00156	lm.nb	0.0113
IKBKG	2.1	0.563	0.00156	lm.nb	0.0113
TREM1	-2.18	0.59	0.00165	lm.nb	0.0118
CD8A	3.13	0.846	0.00166	lm.nb	0.0118
CCL4	1.85	0.503	0.00169	lm.nb	0.0119
TNFSF12	1.91	0.519	0.00175	lm.nb	0.0122
BAD	2.19	0.597	0.00176	lm.nb	0.0122
ITGB2	1.69	0.462	0.00178	lm.nb	0.0122
TRAF1	2.35	0.644	0.00181	lm.nb	0.0122
VSIR	1.87	0.511	0.00181	lm.nb	0.0122
NECTIN2	1.86	0.512	0.00187	lm.nb	0.0125
CX3CL1	1.66	0.462	0.00204	lm.nb	0.0135
TNFRSF14	1.68	0.466	0.00206	lm.nb	0.0135
CD47	1.6	0.445	0.00213	lm.nb	0.0138
CCL5	2.36	0.667	0.00232	lm.nb	0.0149
APOE	2.29	0.653	0.00249	lm.nb	0.0159
TAPBPL	1.38	0.394	0.00253	lm.nb	0.0159
PNOC	2.49	0.707	0.00266	Wald	0.0166
PDGFRB	2.6	0.748	0.00268	lm.nb	0.0166
CXCL9	2.55	0.735	0.00273	lm.nb	0.0168
TMEM173	1.74	0.502	0.00276	lm.nb	0.0168
CD45RO	1.92	0.555	0.0028	lm.nb	0.0169
PTGER4	1.66	0.482	0.00288	lm.nb	0.0172
C1QB	1.82	0.527	0.0029	lm.nb	0.0172
IFNGR2	1.55	0.453	0.00306	lm.nb	0.018
TREM2	2.02	0.592	0.00313	lm.nb	0.0183
LAG3	2.1	0.618	0.00324	lm.nb	0.0188
CEBPB	1.83	0.543	0.00347	lm.nb	0.0199
TGFB3	2.78	0.83	0.00356	lm.nb	0.0203
DLL1	2.02	0.604	0.00368	lm.nb	0.0208
CD3E	2.36	0.709	0.0037	lm.nb	0.0208
TLR7	2.25	0.671	0.00374	Wald	0.0208
IL2RA	1.78	0.535	0.00376	lm.nb	0.0208
HLA-E	1.25	0.376	0.00384	lm.nb	0.0209
GLUD1	1.63	0.491	0.00384	lm.nb	0.0209
EGFR	-1.67	0.505	0.00394	lm.nb	0.0211
CCND3	1.73	0.525	0.00408	lm.nb	0.0214
MMP9	2.72	0.828	0.00412	lm.nb	0.0214
BRD4	1.02	0.311	0.00416	lm.nb	0.0214
MAP3K7	1.55	0.473	0.00421	lm.nb	0.0214
BCAT1	-1.7	0.52	0.00422	lm.nb	0.0214

DEG	Log2 fold change	SD	P-value	Method	Corrected P-value
ITGAX	1.75	0.536	0.00422	lm.nb	0.0214
TAPBP	1.6	0.49	0.00426	lm.nb	0.0214
ITGA4	1.79	0.548	0.00428	lm.nb	0.0214
HLA-A	2.14	0.657	0.00432	lm.nb	0.0215
BCL2L1	1.26	0.388	0.00438	lm.nb	0.0216
RSAD2	2.04	0.632	0.00461	lm.nb	0.0225
IFIH1	1.11	0.343	0.00462	lm.nb	0.0225
BRIP1	1.3	0.404	0.00475	lm.nb	0.023
IFI35	1.69	0.529	0.00503	lm.nb	0.0241
HLA-B	2.02	0.632	0.00505	lm.nb	0.0241
MYD88	0.857	0.269	0.00514	lm.nb	0.0243
GBP2	1.61	0.507	0.00519	lm.nb	0.0244
HERC6	1.8	0.57	0.00542	lm.nb	0.0253
IRF5	1.22	0.387	0.00555	lm.nb	0.0257
MFNG	1.56	0.496	0.00557	lm.nb	0.0257
ICAM3	1.31	0.42	0.00588	lm.nb	0.027
OAS3	1.03	0.329	0.00592	lm.nb	0.027
TNF	1.78	0.571	0.00597	lm.nb	0.027
OAS1	1.03	0.332	0.00601	lm.nb	0.027
MAGEA1	-2.29	0.732	0.00617	Wald	0.0276
PSMB9	1.72	0.556	0.00627	lm.nb	0.0276
VEGFA	1.8	0.582	0.00627	lm.nb	0.0276
CXCL10	2.06	0.668	0.0063	lm.nb	0.0276
APC	1.45	0.472	0.00647	lm.nb	0.0282
BMP2	-1.47	0.477	0.00654	lm.nb	0.0283
DUSP2	1.59	0.52	0.0067	lm.nb	0.0288
IRF9	1.08	0.353	0.00682	lm.nb	0.0292
GBP1	1.41	0.463	0.00697	lm.nb	0.0296
CDKN2A	2.81	0.935	0.00756	lm.nb	0.032
NKG7	2.18	0.726	0.00765	lm.nb	0.0322
OAS2	1.26	0.422	0.00794	lm.nb	0.0329
MARCO	2.47	0.823	0.00797	Wald	0.0329
BRCA2	1.11	0.373	0.00798	lm.nb	0.0329
IFITM1	1.2	0.407	0.00874	lm.nb	0.0359
CXCL6	-2.82	0.964	0.00904	lm.nb	0.0368
CD69	1.37	0.471	0.00919	lm.nb	0.0368
ICAM1	1.02	0.351	0.0092	lm.nb	0.0368
GIMAP4	1.37	0.47	0.00921	lm.nb	0.0368
PARP4	1.14	0.391	0.00925	lm.nb	0.0368
SNAI1	1.74	0.597	0.00929	lm.nb	0.0368
CASP9	1.12	0.386	0.00941	lm.nb	0.0371
CD3G	2.14	0.738	0.00952	lm.nb	0.0371
GPSM3	1.38	0.476	0.0096	lm.nb	0.0371
P4HA2	-3.58	1.24	0.00963	loglinear	0.0371
SGK1	1.58	0.547	0.00974	lm.nb	0.0371
MXI1	1.81	0.626	0.00975	lm.nb	0.0371
FYN	1.16	0.404	0.00993	lm.nb	0.0375
CD4	1.44	0.503	0.0102	lm.nb	0.0383
FAP	-1.33	0.463	0.0104	lm.nb	0.0385

Supplemental Table 4C *Continued*

DEG	Log2 fold change	SD	P-value	Method	Corrected P-value
MYC	1.23	0.433	0.0105	lm.nb	0.0389
C1QA	1.3	0.458	0.0106	lm.nb	0.0389
ITGAM	1.61	0.566	0.0106	lm.nb	0.0389
PALMD	2.11	0.744	0.0109	lm.nb	0.0397
IL2RB	1.59	0.561	0.0111	lm.nb	0.0402
IL11	-2.33	0.825	0.0112	lm.nb	0.0402
SH2D1A	2.22	0.787	0.0113	lm.nb	0.0404
BCL2	1.81	0.643	0.0113	lm.nb	0.0404
STAT1	1.15	0.41	0.0116	lm.nb	0.0409
SOX2	2.38	0.848	0.0116	lm.nb	0.0409
MKI67	1.18	0.421	0.0117	lm.nb	0.0411
TIGIT	1.92	0.687	0.012	lm.nb	0.0418
HIF1A	-1.02	0.368	0.0122	lm.nb	0.0423
HES1	1.11	0.4	0.0122	lm.nb	0.0423
FCGRT	1.28	0.463	0.0128	lm.nb	0.0437
MMP7	-2.39	0.866	0.0129	lm.nb	0.0437
CXCL14	-1.76	0.636	0.0129	lm.nb	0.0437
CXCL5	-4.06	1.47	0.0129	loglinear	0.0437
CD2	1.14	0.412	0.0131	lm.nb	0.044
COL6A3	-1.03	0.377	0.0134	lm.nb	0.0449
FZD8	2.03	0.741	0.0139	Wald	0.0463
CD14	1.37	0.504	0.014	lm.nb	0.0463
CXCL3	-1.65	0.608	0.0141	lm.nb	0.0467
IL1R2	2.28	0.841	0.0143	lm.nb	0.0469
NDUFA4L2	2.02	0.748	0.0148	lm.nb	0.0483

*Differentially expressed genes (DEGs) that are upregulated in (**A**) HPV16^{+}IR^{+} compared to HPV16^{+}IR^{-} OPSCC, (**B**) HPV16+IR+ compared to HPV- OPSCC and (**C**) HPV16+IR- compared to HPV- OPSCC are given as a positive log2 fold change value, while downregulated DEGs are indicated as a negative log2 fold change value. The standard deviation (SD), P-value and corrected P-value (method lm.nb, linear model.negative binomial or Wald) is given for each DEG.*

Supplemental Table 5. Imaging mass cytometry clusters and superclusters.

Supercluster number	Supercluster name	Cluster number	Cluster name
sc01	HLADR+ tumor cell	**c11**	11_HLADR+_Ki67+_D240+_P16+_Bcat+_Ker+_tumor_cell
		c23	23_HLADR+_Bcat+_Ker+_tumor_cell
sc02	HLADR-Ki67+ tumor cell	**c26**	26_Ki67+_D240+_TGFb+_Bcat+_Ker+_tumor_cell
		c28	28_Ki67+_Bcat+_Ker+_tumor_cell
		c30	30_Ki67+_D240+_P16+_Bcat+_Ker+_tumor_cell
		c31	31_Ki67+_TGFb+_P16+_Bcat+_Ker+_tumor_cell
sc03	HLADR-Ki67- tumor cell	**c07**	07_CD103+_Bcat+_Ker+_tumor_cell
		c24	24_P16+_Bcat+_Ker+_tumor_cell
		c25	25_D240+_Bcat+_Ker+_tumor_cell
		c27	27_TGFb+_Bcat+_Ker+_tumor_cell
		c40	40_VISTA+_CD103+_Bcat+_Ker+_tumor_cell
		c46	46_PDL1+_P16+_Bcat+_Ker+_tumor_cell
		c47	47_IDO+_PDL1+_P16+_Bcat+_Ker+_tumor_cell
		c50	50_Caspase+_Bcat+_Ker+_tumor_cell
sc04	CD3+CD4+ FOXP3- T cell	**c01**	01_CD3+_CD4+_CD7+_ICOS+_CD45ro+_T_cell
		c05	05_CD3+_CD4+_VISTA+_CD73+_CD38+_CD45ro+_T_cell
		c14	14_CD3+_CD4+_CD7+_CD45ro+_T_cell
		c34	34_CD3+_CD4+_CD7+_CD73+_CD38+_TGFb+_CD45ro+_T_cell
		c35	35_CD3+_CD4+_CD7+_CD73+_TGFb+_CD45ro+_T_cell
		c37	37_CD3+_CD4+_CD7+_ICOS+_CD103+_D240+_CD45ro+_T_cell
sc05	CD3+CD4+ FOXP3+ Treg	**c42**	42_CD3+_CD4+_CD7+_FOXP3+_CD45ro+_D240+_Treg
		c43	43_CD3+_CD4+_CD7+_FOXP3+_ICOS+_CD45ro+_Treg
sc06	CD3+CD8+ T cell	**c03**	03_CD3+_CD8+_CD4+_CD57+_CD7+_CD45ro+_T_cell
		c04	04_CD3+_CD8+_CD7+_CD103+_CD45ro+_T_cell
		c36	36_CD3+_CD8+_CD7+_TGFb+_CD45ro+_T_cell
sc07	CD20+HLADR+ B cell	**c02**	02_CD20+_HLADR+_CD57+_ CD45ro+_ B_cell
		c41	41_CD20+_HLADR+_Ki67+_CD45+_B_cell
sc08	CD56+ NK cell	**c08**	08_CD56+_CD73+_VISTA+_NK_cell
sc09	CD3-CD7+ ILC	**c06**	06_CD7+_CD73+_TGFb+_ILC
sc10	CD11b+CD15+ granulocyte	**c48**	48_CD11b+_CD15+_VISTA+_CD45ro+_granulocyte
		c49	49_CD11b+_CD15+_CD45ro+_granulocyte
sc11	CD11c+CD14+ HLADR+ DC	**c12**	12_CD11c+_CD14+_HLADR+_D240+_CD45ro+_DC
		c13	13_CD11c+_CD14+_HLADR+_CD45ro+_DC

Supplemental Table 5 *Continued*

Supercluster number	Supercluster name	Cluster number	Cluster name
sc12	CD68+CD163- M1 macrophage	**c15**	15_CD68+_CD14+_CD204+_HLADR+_TGFb+_ macrophage
		c32	32_CD68+_VISTA+_CD38+_CD31+_ macrophage
		c38	38_CD68+_CD14+_CD204+_CD11c+_HLADR+_ macrophage
sc13	CD68+CD163+ M2 macrophage	**c39**	39_CD68+_CD163+_CD14+_CD204+_CD11c+_ HLADR+_macrophage
		c44	44_CD68+_CD163+_CD14+_CD11c+_HLADR+_ VISTA+_macrophage
		c45	45_CD68+_CD163+_CD14+_VISTA+_CD38+_ CD31+_macrophage
		c51	51_CD68+_CD163+_macrophage
sc14	CD68- CD14+HLADR+ myeloid cell	**c16**	16_CD14+_ CD204+_HLADR+_ CD45ro+_ myeloid_cell
		c17	17_CD14+_HLADR+_CD73+_TGFb+_myeloid_ cell
sc15	CD45ro+lin- memory immune cell	**c22**	22_CD45ro+_memory_immune_cell
		c29	29_HLADR+_CD45ro+_memory_immune_cell
sc16	Vim+lin- fibroblast	**c18**	18_TGFb+_Vim+_fibroblast
		c19	19_Vim+_fibroblast
		c20	20_Vim+_D240+_fibroblast
sc17	CD38+Vim+lin- stromal cell	**c21**	21_CD38+_stromal_cell
		c33	33_CD38+_CD31+_CD73+_TGFb+_stromal_cell
sc18	CD31+ blood vessel endothelial cell	**c09**	09_CD31+_CD73+_blood_vessel
		c10	10_CD31+_CD73+_TGFb+_blood_vessel
sc19	D240+ tumor cell	**c11**	11_HLADR+_Ki67+_D240+_P16+_Bcat+_Ker+_ tumor_cell
		c25	25_D240+_Bcat+_Ker+_tumor_cell
		c26	26_Ki67+_D240+_TGFb+_Bcat+_Ker+_tumor_ cell
		c30	30_Ki67+_D240+_P16+_Bcat+_Ker+_tumor_ cell
sc20	CD103+ tumor cell	**c07**	07_CD103+_Bcat+_Ker+_tumor_cell
		c40	40_VISTA+_CD103+_Bcat+_Ker+_tumor_cell
sc21	Ki67+ tumor cell	**c11**	11_HLADR+_Ki67+_D240+_P16+_Bcat+_Ker+_ tumor_cell
		c26	26_Ki67+_D240+_TGFb+_Bcat+_Ker+_tumor_ cell
		c28	28_Ki67+_Bcat+_Ker+_tumor_cell
		c30	30_Ki67+_D240+_P16+_Bcat+_Ker+_tumor_ cell
		c31	31_Ki67+_TGFb+_P16+_Bcat+_Ker+_tumor_cell

Supercluster number	Supercluster name	Cluster number	Cluster name
sc22	CD3+FOXP3-TGFb+ T cell	**c34**	34_CD3+_CD4+_CD7+_CD73+_CD38+_TGFb+_CD45ro+_Th_cell
		c35	35_CD3+_CD4+_CD7+_CD73+_TGFb+_CD45ro+_T_cell
		c36	36_CD3+_CD8+_CD7+_TGFb+_CD45ro+_Tc_cell
sc23	CD11c+ cell	**c12**	12_CD11c+_CD14+_HLADR+_D240+_CD45ro+_DC
		c13	13_CD11c+_CD14+_HLADR+_CD45ro+_DC
		c38	38_CD68+_CD14+_CD204+_CD11c+_HLADR+_macrophage
sc24	CD38+CD31+ stromal cell	**c32**	32_CD68+_VISTA+_CD38+_CD31+_macrophage
		c33	33_CD38+_CD31+_CD73+_TGFb+_stromal_cell
		c45	45_CD68+_CD163+_CD14+_VISTA+_CD38+_CD31+_macrophage
sc25	CD103+ T cell	**c37**	37_CD3+_CD4+_CD7+_ICOS+_CD103+_D240+_CD45ro+_Th_cell
		c04	04_CD3+_CD8+_CD7+_CD103+_CD45ro+_Tc_cell
sc26	ICOS+ T cell	**c01**	01_CD3+_CD4+_CD7+_ICOS+_CD45ro+_Th_cell
sc27	TGFb+ myeloid cell	**c15**	15_CD68+_CD14+_CD204+_HLADR+_TGFb+_macrophage
		c17	17_CD14+_HLADR+_CD73+_TGFb+_myeloid_cell
sc28	CD14+ myeloid cell	**c12**	12_CD11c+_CD14+_HLADR+_D240+_CD45ro+_DC
		c13	13_CD11c+_CD14+_HLADR+_CD45ro+_DC
		c15	15_CD68+_CD14+_CD204+_HLADR+_TGFb+_macrophage
		c38	38_CD68+_CD14+_CD204+_CD11c+_HLADR+_macrophage
		c39	39_CD68+_CD163+_CD14+_CD204+_CD11c+_HLADR+_macrophage
		c44	44_CD68+_CD163+_CD14+_CD11c+_HLADR+_VISTA+_macrophage
		c45	45_CD68+_CD163+_CD14+_VISTA+_CD38+_CD31+_macrophage
		c16	16_CD14+_ CD204+_HLADR+_ CD45ro+_myeloid_cell
		c17	17_CD14+_HLADR+_CD73+_TGFb+_myeloid_cell

Cluster name is based on the markers that are expressed by that cluster, indicating that that cluster is negative for all other tested markers that are not mentioned in the cluster name.

Supplemental Table 6. Single cell sequencing counts per identified cluster.

	H143	H197	H205	H149	H182	H208	H211	H141	H160	H176	H185	H188	H68
Cluster	HPV-	HPV-	HPV-	HPV+ IR-	HPV+IR-	HPV+IR-	HPV+IR-	HPV+IR+	HPV+IR+	HPV+IR+	HPV+IR+	HPV+IR+	HPV+IR+
CD8_0	31*	66	10	5	45	10	15	19	73	50	302	184	49
CD8_1	276	7	10	10	90	8	23	63	81	70	54	18	64
CD8_2	446	2	5	2	12	0	6	8	32	10	14	6	1
CD8_3	0	71	6	0	7	41	2	0	10	83	65	18	212
CD8_4	9	8	4	17	96	2	11	7	9	33	81	205	33
CD8_5	7	87	9	10	15	15	10	21	11	30	90	132	15
CD8_6	0	15	2	1	9	316	2	2	5	15	17	24	22
CD8_7	1	1	1	9	11	3	4	12	1	12	7	40	305
CD8_8	0	0	0	0	8	5	4	2	3	4	8	26	255
CD8_9	2	2	1	0	0	5	3	0	1	101	0	0	151
CD8_10	0	16	3	0	2	45	0	1	1	10	13	4	38
CD8_11	1	19	1	0	3	5	1	0	6	1	0	2	0
CD4_0	2	0	4	202	51	5	28	7	1	33	40	324	224
CD4_1	103	12	53	87	82	7	78	48	251	23	136	8	11
CD4_2	3	17	12	9	98	172	28	27	10	33	14	82	379
CD4_3	203	0	43	74	52	1	175	96	104	2	16	5	3
CD4_4	17	2	15	11	15	16	112	516	13	9	8	8	22
CD4_5	16	61	19	47	81	7	32	34	24	45	113	239	42
CD4_6	9	3	33	309	54	0	5	19	8	11	85	16	8
CD4_7	19	46	16	15	40	41	44	22	87	113	53	21	10
CD4_8	11	99	8	8	26	41	7	10	16	34	38	90	100
CD4_9	38	6	14	3	54	19	74	39	93	95	7	3	14

	H143	H197	H205	H149	H182	H208	H211	H141	H160	H176	H185	H188	H68
Cluster	**HPV-**	**HPV-**	**HPV-**	**HPV+ IR-**	**HPV+IR-**	**HPV+IR-**	**HPV+IR-**	**HPV+IR+**	**HPV+IR+**	**HPV+IR+**	**HPV+IR+**	**HPV+IR+**	**HPV+IR+**
CD4_10	2	3	0	0	0	2	0	2	6	29	0	4	107
Treg_0	4	67	8	17	46	23	31	71	31	58	61	101	116
Treg_1	3	20	6	6	41	94	7	5	7	42	15	51	102
Treg_2	0	7	0	0	4	181	4	10	0	7	0	7	13
Treg_3	0	141	1	0	4	3	0	0	0	2	2	1	3
Treg_4	0	16	3	3	18	38	8	5	10	20	5	8	21
Treg_5	0	0	0	0	0	5	0	0	0	25	1	1	36
Tother_0	18	0	4	0	23	2	13	10	8	2	9	11	3
Tother_1	2	0	7	0	11	1	1	4	0	0	0	3	5
Tother_2	1	0	1	3	5	1	1	2	1	0	0	3	0
NK_0	2	21	21	46	149	14	20	16	28	78	59	97	272
NK_1	1	222	8	6	46	34	14	11	42	55	288	35	22
NK_2	0	12	1	1	9	586	0	22	0	9	6	5	11
NK_3	2	5	13	7	54	22	40	19	37	16	13	8	8
NK_4	0	146	5	1	13	18	4	4	6	8	6	7	14
NK_5	0	0	1	0	0	2	0	0	1	36	2	0	35

** Number of cells identified per patient in each cluster.*

References

1. Shield KD, Ferlay J, Jemal A, et al. The global incidence of lip, oral cavity, and pharyngeal cancers by subsite in 2012. *CA: a cancer journal for clinicians* 2017;67(1):51-64.
2. Welters MJ, Ma W, Santegoets SJ, et al. Intratumoral HPV16-specific T cells constitute a type I–oriented tumor microenvironment to improve survival in HPV16-driven oropharyngeal cancer. *Clinical Cancer Research* 2018;24(3):634-47.
3. Ang KK, Harris J, Wheeler R, et al. Human papillomavirus and survival of patients with oropharyngeal cancer. *New England Journal of Medicine* 2010;363(1):24-35.
4. Pignon J-P, Le Maitre A, Maillard E, et al. Meta-analysis of chemotherapy in head and neck cancer (MACH-NC): an update on 93 randomised trials and 17,346 patients. *Radiotherapy and oncology* 2009;92(1):4-14.
5. Burtness B, Harrington KJ, Greil R, et al. Pembrolizumab alone or with chemotherapy versus cetuximab with chemotherapy for recurrent or metastatic squamous cell carcinoma of the head and neck (KEYNOTE-048): a randomised, open-label, phase 3 study. *The Lancet* 2019;394(10212):1915-28.
6. Ferris RL, Blumenschein Jr G, Fayette J, et al. Nivolumab for recurrent squamous-cell carcinoma of the head and neck. *N Engl J Med* 2016;375:1856-67.
7. Galon J, Bruni D. Approaches to treat immune hot, altered and cold tumours with combination immunotherapies. *Nat Rev Drug Discov* 2019;18(3):197-218. doi: 10.1038/s41573-018-0007-y [published Online First: 2019/01/06]
8. Tumeh PC, Harview CL, Yearley JH, et al. PD-1 blockade induces responses by inhibiting adaptive immune resistance. *Nature* 2014;515(7528):568-71. doi: 10.1038/nature13954 [published Online First: 2014/11/28]
9. Zou W, Wolchok JD, Chen L. PD-L1 (B7-H1) and PD-1 pathway blockade for cancer therapy: Mechanisms, response biomarkers, and combinations. *Sci Transl Med* 2016;8(328):328rv4. doi: 10.1126/scitranslmed.aad7118 [published Online First: 2016/03/05]
10. Kumagai S, Togashi Y, Kamada T, et al. The PD-1 expression balance between effector and regulatory T cells predicts the clinical efficacy of PD-1 blockade therapies. *Nat Immunol* 2020;21(11):1346-58. doi: 10.1038/s41590-020-0769-3 [published Online First: 2020/09/02]
11. Network CGA. Comprehensive genomic characterization of head and neck squamous cell carcinomas. *Nature* 2015;517(7536):576.
12. Santegoets SJ, van Ham VJ, Ehsan I, et al. The anatomical location shapes the immune infiltrate in tumors of same etiology and affects survival. *Clinical Cancer Research* 2019;25(1):240-52.
13. Ijsselsteijn ME, van der Breggen R, Farina Sarasqueta A, et al. A 40-Marker Panel for High Dimensional Characterization of Cancer Immune Microenvironments by Imaging Mass Cytometry. *Front Immunol* 2019;10:2534. doi: 10.3389/fimmu.2019.02534 [published Online First: 2019/11/19]
14. Schapiro D, Jackson HW, Raghuraman S, et al. histoCAT: analysis of cell phenotypes and interactions in multiplex image cytometry data. *Nat Methods* 2017;14(9):873-76. doi: 10.1038/nmeth.4391 [published Online First: 2017/08/08]
15. Somarakis A, Van Unen V, Koning F, et al. ImaCytE: Visual Exploration of Cellular Micro-Environments for Imaging Mass Cytometry Data. *IEEE Trans Vis Comput Graph* 2021;27(1):98-110. doi: 10.1109/tvcg.2019.2931299 [published Online First: 2019/08/02]
16. van Unen V, Höllt T, Pezzotti N, et al. Visual analysis of mass cytometry data by hierarchical stochastic neighbour embedding reveals rare cell types. *Nat Commun* 2017;8(1):1740. doi: 10.1038/s41467-017-01689-9 [published Online First: 2017/11/25]
17. Kortekaas KE, Santegoets SJ, Sturm G, et al. CD39 Identifies the CD4(+) Tumor-Specific T-cell Population in Human Cancer. *Cancer Immunol Res* 2020;8(10):1311-21. doi: 10.1158/2326-6066.Cir-20-0270 [published Online First: 2020/08/08]
18. Wolf FA, Angerer P, Theis FJ. SCANPY: large-scale single-cell gene expression data analysis. *Genome biology* 2018;19(1):1-5.
19. Sturm G, Szabo T, Fotakis G, et al. Scirpy: a Scanpy extension for analyzing single-cell T-cell receptor-sequencing data. *Bioinformatics* 2020;36(18):4817-18.
20. Bernstein NJ, Fong NL, Lam I, et al. Solo: Doublet Identification in Single-Cell RNA-Seq via Semi-Supervised Deep Learning. *Cell Syst* 2020;11(1):95-101.e5. doi: 10.1016/j.cels.2020.05.010 [published Online First: 2020/06/28]

21. Traag VA, Waltman L, Van Eck NJ. From Louvain to Leiden: guaranteeing well-connected communities. *Scientific reports* 2019;9(1):1-12.
22. McInnes L, Healy J, Melville J. Umap: Uniform manifold approximation and projection for dimension reduction. *arXiv preprint arXiv:180203426* 2018
23. Robinson MD, McCarthy DJ, Smyth GK. edgeR: a Bioconductor package for differential expression analysis of digital gene expression data. *Bioinformatics* 2010;26(1):139-40.
24. Ge Z, Ding S. The Crosstalk Between Tumor-Associated Macrophages (TAMs) and Tumor Cells and the Corresponding Targeted Therapy. *Front Oncol* 2020;10:590941. doi: 10.3389/fonc.2020.590941 [published Online First: 2020/11/24]
25. Gabellini C, Trisciuoglio D, Desideri M, et al. Functional activity of CXCL8 receptors, CXCR1 and CXCR2, on human malignant melanoma progression. *Eur J Cancer* 2009;45(14):2618-27. doi: 10.1016/j.ejca.2009.07.007 [published Online First: 2009/08/18]
26. Zhao HJ, Chang HM, Zhu H, et al. Bone Morphogenetic Protein 2 Promotes Human Trophoblast Cell Invasion by Inducing Activin A Production. *Endocrinology* 2018;159(7):2815-25. doi: 10.1210/en.2018-00301 [published Online First: 2018/05/31]
27. Huynh J, Baloyan D, Chisanga D, et al. Host IL-11 signaling suppresses CD4+ T cell-mediated anti-tumor responses to colon cancer in mice. *Cancer Immunol Res* 2021 doi: 10.1158/2326-6066.Cir-19-1023 [published Online First: 2021/04/29]
28. Pitzalis C, Jones GW, Bombardieri M, et al. Ectopic lymphoid-like structures in infection, cancer and autoimmunity. *Nature Reviews Immunology* 2014;14(7):447-62.
29. Bindea G, Mlecnik B, Hackl H, et al. ClueGO: a Cytoscape plug-in to decipher functionally grouped gene ontology and pathway annotation networks. *Bioinformatics* 2009;25(8):1091-3. doi: 10.1093/bioinformatics/btp101 [published Online First: 2009/02/25]
30. Das R, Coupar J, Clavijo PE, et al. Lymphotoxin-β receptor-NIK signaling induces alternative RELB/NF-κB2 activation to promote metastatic gene expression and cell migration in head and neck cancer. *Mol Carcinog* 2019;58(3):411-25. doi: 10.1002/mc.22938 [published Online First: 2018/11/30]
31. Bindea G, Mlecnik B, Tosolini M, et al. Spatiotemporal dynamics of intratumoral immune cells reveal the immune landscape in human cancer. *Immunity* 2013;39(4):782-95. doi: 10.1016/j.immuni.2013.10.003 [published Online First: 2013/10/22]
32. Ali HR, Jackson HW, Zanotelli VR, et al. Imaging mass cytometry and multiplatform genomics define the phenogenomic landscape of breast cancer. *Nature Cancer* 2020;1(2):163-75.
33. Pasetto A, Gros A, Robbins PF, et al. Tumor- and Neoantigen-Reactive T-cell Receptors Can Be Identified Based on Their Frequency in Fresh Tumor. *Cancer Immunol Res* 2016;4(9):734-43. doi: 10.1158/2326-6066.Cir-16-0001 [published Online First: 2016/06/30]
34. Charoentong P, Finotello F, Angelova M, et al. Pan-cancer immunogenomic analyses reveal genotype-immunophenotype relationships and predictors of response to checkpoint blockade. *Cell reports* 2017;18(1):248-62.
35. Galeano Niño JL, Pageon SV, Tay SS, et al. Cytotoxic T cells swarm by homotypic chemokine signalling. *Elife* 2020;9 doi: 10.7554/eLife.56554 [published Online First: 2020/10/14]
36. Spranger S, Bao R, Gajewski TF. Melanoma-intrinsic β-catenin signalling prevents anti-tumour immunity. *Nature* 2015;523(7559):231-5. doi: 10.1038/nature14404 [published Online First: 2015/05/15]
37. Garris CS, Arlauckas SP, Kohler RH, et al. Successful Anti-PD-1 Cancer Immunotherapy Requires T Cell-Dendritic Cell Crosstalk Involving the Cytokines IFN-γ and IL-12. *Immunity* 2018;49(6):1148-61.e7. doi: 10.1016/j.immuni.2018.09.024 [published Online First: 2018/12/16]
38. Luther SA, Bidgol A, Hargreaves DC, et al. Differing activities of homeostatic chemokines CCL19, CCL21, and CXCL12 in lymphocyte and dendritic cell recruitment and lymphoid neogenesis. *The Journal of Immunology* 2002;169(1):424-33.
39. Matsuo K, Kitahata K, Kawabata F, et al. A Highly Active Form of XCL1/Lymphotactin Functions as an Effective Adjuvant to Recruit Cross-Presenting Dendritic Cells for Induction of Effector and Memory CD8(+) T Cells. *Front Immunol* 2018;9:2775. doi: 10.3389/fimmu.2018.02775 [published Online First: 2018/12/14]
40. Mukaida N, Sasaki SI, Baba T. CCL4 Signaling in the Tumor Microenvironment. *Adv Exp Med Biol* 2020;1231:23-32. doi: 10.1007/978-3-030-36667-4_3 [published Online First: 2020/02/16]

41. González-Granado JM, Silvestre-Roig C, Rocha-Perugini V, et al. Nuclear envelope lamin-A couples actin dynamics with immunological synapse architecture and T cell activation. *Sci Signal* 2014;7(322):ra37. doi: 10.1126/scisignal.2004872 [published Online First: 2014/04/24]
42. Toribio-Fernández R, Zorita V, Rocha-Perugini V, et al. Lamin A/C augments Th1 differentiation and response against vaccinia virus and Leishmania major. *Cell Death Dis* 2018;9(1):9. doi: 10.1038/s41419-017-0007-6 [published Online First: 2018/01/10]
43. Lee JS, Yi K, Ju YS, et al. Effects of Cryopreservation and Thawing on Single-Cell Transcriptomes of Human T Cells. *Immune Netw* 2020;20(4):e34. doi: 10.4110/in.2020.20.e34 [published Online First: 2020/09/09]
44. Koster BD, López González M, van den Hout MF, et al. T cell infiltration on local CpG-B delivery in early-stage melanoma is predominantly related to CLEC9A(+)CD141(+) cDC1 and CD14(+) antigen-presenting cell recruitment. *J Immunother Cancer* 2021;9(3) doi: 10.1136/jitc-2020-001962 [published Online First: 2021/03/20]
45. Jardine L, Cytlak U, Gunawan M, et al. Donor monocyte-derived macrophages promote human acute graft-versus-host disease. *J Clin Invest* 2020;130(9):4574-86. doi: 10.1172/jci133909 [published Online First: 2020/05/27]
46. de Vos van Steenwijk PJ, Ramwadhdoebe TH, Goedemans R, et al. Tumor-infiltrating CD14-positive myeloid cells and CD8-positive T-cells prolong survival in patients with cervical carcinoma. *Int J Cancer* 2013;133(12):2884-94. doi: 10.1002/ijc.28309 [published Online First: 2013/06/07]
47. Abdulrahman Z, de Miranda N, Hellebrekers BWJ, et al. A pre-existing coordinated inflammatory microenvironment is associated with complete response of vulvar high-grade squamous intraepithelial lesions to different forms of immunotherapy. *Int J Cancer* 2020;147(10):2914-23. doi: 10.1002/ijc.33168 [published Online First: 2020/06/24]
48. Abdulrahman Z, de Miranda N, van Esch EMG, et al. Pre-existing inflammatory immune microenvironment predicts the clinical response of vulvar high-grade squamous intraepithelial lesions to therapeutic HPV16 vaccination. *J Immunother Cancer* 2020;8(1) doi: 10.1136/jitc-2020-000563 [published Online First: 2020/03/15]
49. Beyranvand Nejad E, Labrie C, Abdulrahman Z, et al. Lack of myeloid cell infiltration as an acquired resistance strategy to immunotherapy. *J Immunother Cancer* 2020;8(2) doi: 10.1136/jitc-2020-001326 [published Online First: 2020/09/03]
50. Helmink BA, Reddy SM, Gao J, et al. B cells and tertiary lymphoid structures promote immunotherapy response. *Nature* 2020;577(7791):549-55. doi: 10.1038/s41586-019-1922-8 [published Online First: 2020/01/17]
51. Cabrita R, Lauss M, Sanna A, et al. Tertiary lymphoid structures improve immunotherapy and survival in melanoma. *Nature* 2020;577(7791):561-65. doi: 10.1038/s41586-019-1914-8 [published Online First: 2020/01/17]
52. Flavell RA, Sanjabi S, Wrzesinski SH, et al. The polarization of immune cells in the tumour environment by TGFbeta. *Nat Rev Immunol* 2010;10(8):554-67. doi: 10.1038/nri2808 [published Online First: 2010/07/10]
53. Engblom C, Pfirschke C, Pittet MJ. The role of myeloid cells in cancer therapies. *Nat Rev Cancer* 2016;16(7):447-62. doi: 10.1038/nrc.2016.54 [published Online First: 2016/06/25]
54. Yi H, Zuo D, Yu X, et al. Suppression of antigen-specific CD4+ T cell activation by SRA/CD204 through reducing the immunostimulatory capability of antigen-presenting cell. *J Mol Med (Berl)* 2012;90(4):413-26. doi: 10.1007/s00109-011-0828-1 [published Online First: 2011/11/16]
55. Ferris RL, Blumenschein Jr G, Fayette J, et al. Nivolumab vs investigator's choice in recurrent or metastatic squamous cell carcinoma of the head and neck: 2-year long-term survival update of CheckMate 141 with analyses by tumor PD-L1 expression. *Oral oncology* 2018;81:45-51.
56. Massarelli E, William W, Johnson F, et al. Combining immune checkpoint blockade and tumor-specific vaccine for patients with incurable human papillomavirus 16–related cancer: a phase 2 clinical trial. *JAMA oncology* 2019;5(1):67-73.

57. Li H, Li L, Mei H, et al. Antitumor properties of triptolide: phenotype regulation of macrophage differentiation. *Cancer Biol Ther* 2020;21(2):178-88. doi: 10.1080/15384047.2019.1679555 [published Online First: 2019/10/31]
58. Tauriello DVF, Palomo-Ponce S, Stork D, et al. TGFβ drives immune evasion in genetically reconstituted colon cancer metastasis. *Nature* 2018;554(7693):538-43. doi: 10.1038/nature25492 [published Online First: 2018/02/15]
59. McDermott DF, Huseni MA, Atkins MB, et al. Clinical activity and molecular correlates of response to atezolizumab alone or in combination with bevacizumab versus sunitinib in renal cell carcinoma. *Nat Med* 2018;24(6):749-57. doi: 10.1038/s41591-018-0053-3 [published Online First: 2018/06/06]